

JUL 23 1958

NATIONAL ADVISORY COMMITTEE FOR AERONAUTICS

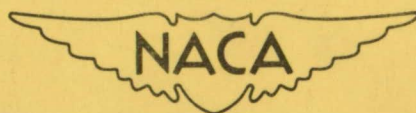
TECHNICAL NOTE 4253

DESIGN AND TESTS OF A SIX-STAGE AXIAL-FLOW COMPRESSOR
HAVING A TIP SPEED OF 550 FEET PER SECOND
AND A FLAT OPERATING CHARACTERISTIC
AT CONSTANT SPEED

By Willard R. Westphal and John W. Maynard, Jr.

Langley Aeronautical Laboratory
Langley Field, Va.

PROPERTY FAIRCHILD
ENGINEERING LIBRARY



Washington
June 1958

NATIONAL ADVISORY COMMITTEE FOR AERONAUTICS

TECHNICAL NOTE 4253

DESIGN AND TESTS OF A SIX-STAGE AXIAL-FLOW COMPRESSOR

HAVING A TIP SPEED OF 550 FEET PER SECOND

AND A FLAT OPERATING CHARACTERISTIC

AT CONSTANT SPEED

By Willard R. Westphal and John W. Maynard, Jr.

SUMMARY

A six-stage axial-flow compressor with a tip speed of 550 feet per second and a flat operating characteristic at constant speed has been designed and tested. It was designed for a constant power input per pound of flow in expectation that this would result in a wider mass-flow operating range at a given stagnation-pressure ratio. The design specific weight flow was 21.3 pounds per second per square foot of frontal area at atmospheric discharge with a stagnation-pressure ratio of 3.25 and an inlet hub-tip radius ratio of 0.7. Several configurations consisting of various blade setting angles and solidities were tested. Tests showed that the design flow, pressure ratio, and flat operating characteristic were obtained over a range of 10 percent of design flow at a peak efficiency of 82 percent for design conditions. The compressor had a possible immediate application for air removal from a large slotted-throat transonic wind tunnel, but the design theory could apply to any low-speed industrial compressor or second spool of a turbojet engine.

INTRODUCTION

The design tip speed of an axial-flow compressor is usually selected as high as possible within the limitation imposed by the drag-rise Mach number relative to the rotor blades since the pressure rise per stage increases exponentially with tip speed for similar blading and flow angles. As a result of considerable research and development effort, the tip speed and pressure ratio of aircraft gas-turbine type of compressors have greatly increased in recent years.

Lower tip speeds have some advantages, such as greater freedom in structural design and blade selection, particularly for industrial-type compressors driven by electric motors, if the pressure ratio per stage can be maintained at a moderately high level. The rear stages of an aircraft jet-engine compressor also operate at low corrected tip speeds because of the temperature rise of the compressed air. For example, at a flight Mach number of 2.5 in the stratosphere and a first-spool pressure ratio of 2.0, a second spool operating at an actual tip speed of 1,000 feet per second would have a corrected tip speed of 675 feet per second. For matching the conditions entering the second spool to those leaving the first spool, a flat operating characteristic in the first spool would ease the problem of selecting the vector diagrams for the second spool. In order to operate an engine at low tip speeds, higher turning angles are required to keep the work input high enough to obtain a desired pressure ratio at reasonable efficiencies. Impulse-type blades meet the above conditions.

References 1 and 2 describe the design and performance of an impulse-type rotor at low speeds with and without a stator blade row. A very high total-pressure-rise coefficient was attained with good efficiency. The static-pressure rise was too low to permit multistaging of similar rotors. The velocity leaving the stage was considerably higher than that entering it. The static-pressure rise divided by the entering relative impact pressure, $\frac{\Delta p}{P_{1,R} - P_{1,R}}$, has been found from cascade data (ref. 3) to be a significant loading-limit parameter for compressor blade rows. The denominator is mainly a function of the rotational speed and the axial velocity. It is possible to increase or decrease the entering impact pressure of the rotor relative to that of the stator by using guide vanes, if the rotational speed and the work done are constant. For a multistage machine where symmetrical vector diagrams are desired for all stages and each stage turns axially, the use of guide vanes is of no particular advantage. In references 1 and 2, a high total-pressure rise was attained without exceeding allowable values of $\frac{\Delta p}{P_{1,R} - P_{1,R}}$. Since the impact pressure

was low, the pressure rise in the rotor was approximately zero; this left too large a static-pressure rise for the following stator and resulted in a high velocity leaving the stage. The present trend in aircraft axial-flow compressors is to increase the entering impact pressure relative to the rotor to high values by designing for supersonic relative inlet velocities. This has been a successful approach particularly at low supersonic velocities. The high relative velocities are attained by raising both axial velocity and rotational speeds. The objective of the present investigation was to obtain information on the performance possible by combining a low rotational speed and a moderately high axial velocity to attain relative Mach numbers in the moderately

high subsonic range. The values chosen result in a relative impact pressure that is high enough to permit pressure ratios of 1.2 per stage with symmetrical stages (both rotor and stator turn axially in their respective coordinates) that have no increase in velocities across the stage and, hence, are suitable for multistaging.

A six-stage compressor of this type was designed, built, and tested. The compressor was designed with a possible immediate application for air removal from a large slotted-throat transonic wind tunnel, but the results are equally applicable to other cases where a low-tip-speed compressor is advantageous. For the air-removal application, the compressor was to be driven by a constant-speed motor and it was advantageous to have a wide quantity-flow operating range at this constant speed and at constant pressure ratio. The compressor was therefore designed for a constant power input per pound of flow with symmetrical vector diagrams at the pitch section in expectation that this would result in a wider quantity-flow operating range.

A multistage compressor with a symmetrical vector diagram for each stage, designed for operation in air, can be operated in gases of other densities without serious mismatching. Freon-12 has a higher density than air and produces a higher weight flow without incurring stall. In order to illustrate the phenomena, the compressor was tested in both air and Freon-12. This investigation was made at the Langley cascade aerodynamics laboratory.

SYMBOLS

C_{l_0}	camber expressed as lift coefficient of isolated airfoil
c_p	specific heat at constant pressure, $\frac{\text{ft-lb}}{\text{slug} \cdot ^\circ\text{R}}$
M	Mach number
m	mass, slugs
n	number of degrees of freedom
P	total pressure, lb/sq ft
p	static pressure, lb/sq ft
Δp	static-pressure rise, $p_2 - p_1$

R_1, R_2, \dots	rotor 1, rotor 2, and so forth
S_1, S_2, \dots	stator 1, stator 2, and so forth
T	stagnation temperature, $^{\circ}R$
U	rotational speed, ft/sec
V	velocity, ft/sec
α	angle between entering flow direction and blade chord, deg
α_{LSC}	angle between entering flow direction and blade chord for optimum conditions from low-speed cascade data, deg
α_{req}	angle between entering flow direction and blade chord required to match previous stage, deg
β	flow angle measured from axial direction, deg
γ	ratio of specific heats
η_Q	efficiency based on torque, $\frac{c_p T_1 \left[\left(\frac{P_2}{P_1} \right)^{\frac{\gamma-1}{\gamma}} - 1 \right]}{\omega [\text{Torque}]_{\text{measured}}}$
η_T	efficiency based on temperature, $\left[\frac{\left(\frac{P_2}{P_1} \right)^{\frac{\gamma-1}{\gamma}} - 1}{T_2 - T_1} \right] T_1$
θ	flow turning angle, deg
ρ	density, slugs/cu ft
σ	solidity, Chord/Spacing ratio
ω	angular velocity, radians/sec

Subscripts:

- 1 entering rotor
- 2 leaving rotor

3	leaving stator
4	leaving stator 6
1	inlet
R	rotor
S	stator
z	axial
θ	tangential

DESIGN

General Vector-Diagram Considerations

The vector diagrams were selected to produce a flat operating characteristic (constant stagnation-pressure ratio over the range of mass flow) at constant speed or, more specifically, to have a constant work input per pound of flow at constant speed independent of the axial velocity. The following equation expressing the rate of change of work input with change in axial velocity is derived in appendix A:

$$\frac{\frac{d(\Delta V_\theta)}{\Delta V_\theta}}{\frac{dV_z}{V_z}} = 1 - \frac{U}{\Delta V_\theta}$$

The following assumptions were made in the derivation:

1. Entering and leaving axial velocities are equal.
2. Streamlines remain at the same radii.
3. Leaving flow direction relative to the rotor remains constant as entering direction varies.

Conventional axial-flow compressors have a rotational speed two or three times as great as the change in tangential velocity and, hence, their constant-speed operating line has a high negative slope. The impulse compressor of references 1 and 2 has a rotational speed less than the change in tangential velocity at some blade setting angles of the tests and, therefore, had an operating line which sloped in a positive direction;

that is, the stagnation-pressure rise increased with increasing quantity flow.

Vector-Diagram Selection

Since an operating-line slope of zero was desired for this compressor, it was necessary to make the change in tangential velocity equal to the rotational speed. This can only be done at one radius if one of the design criteria is that the power input is to be constant radially. The mean radius was chosen as the significant one. A hub-tip radius ratio of 0.7 was selected for the first rotor, since compressor weight and frontal area were not important considerations and it was believed that a high hub-tip radius ratio would give a wider operating range. No guide vanes were used in this compressor. With no guide vanes, both the rotor and stators turned the flow to the axial direction at the mean radius and, hence, the vector diagrams were only symmetrical at that radius. All stages turned axially at all radial stations.

The numerical values of the rotational speed and, hence, pressure ratio per stage were selected by considering blade diffusion limits and the Mach number attainable without choking. The diffusion limit used was the static-pressure rise divided by the relative entering impact

pressures, $\frac{\Delta p}{P_{1,R} - P_{1,R}}$. A maximum value of 0.5 was set from cascade

data for this parameter. The entering impact pressure relative to the rotor was then made as large as practical to attain a high pressure ratio per stage. The relative impact pressure was limited by choking in the throat of the blade passage. The inlet air angles are low and the solidities are high because of the high turning angles required. The solidities and inlet air angles limited the entering Mach number to about 0.77 at the mean radius. Increasing either the axial velocity or the rotational speed was considered equally effective as a means of attaining a high relative impact pressure. In other words, the limiting value of

$\frac{\Delta p}{P_{1,R} - P_{1,R}}$ was considered independent of the rotor inlet air angle.

Because of the interrelation of the many variables, the vector-diagram selection was an iterative process. After several iterations including the trial-blade-section selections necessary to check the choking Mach number, an axial velocity of 650 feet per second and a tip speed of 550 feet per second were selected. The average stagnation-pressure ratio per stage was then 1.22 which permitted the design overall pressure ratio of 3.25 to be attained in six stages. The flow was assumed to be in simple radial equilibrium between blade rows. The vector diagram for the first stage is shown in figure 1 and pertinent numerical values for all stages are given in table I.

The throat area for the first rotor was within 5 percent of the choking value at all radial stations at the design point. No allowance was made for boundary-layer displacement thickness in the inlet and none for boundary-layer growth through the machine except as included in the design efficiency assumption. The design polytropic efficiency based on static pressure and temperature was 85.8 percent. A value of about 85 percent was believed realistic considering that the wakes of one blade row have a considerably lower velocity relative to the following row than is the case in conventional higher-tip-speed compressors. In the conventional compressor, the velocities of the wakes relative to the following blade row are approximately equal in magnitude to that of the free-stream air but at an angle different from that of the free-stream air. In this design, the wakes have a smaller difference in direction and a larger deficit in velocity. This low-energy air is able to continue flowing downstream through the diffuser, that is, the next blade row, only because it receives energy from the free stream by turbulent mixing. This mixing was arbitrarily assumed to result in a 5-percent penalty in efficiency as compared with the usual design value of 90 percent for a more conventional compressor. The exact value of 85.8 percent was chosen because the polytropic exponent of the temperature ratio is then a convenient integer. The adiabatic efficiency for the design pressure ratio of 3.25 was then 82.8 percent.

Blade-Section Selection

NACA $a = 1.0$ (uniform loading on isolated airfoils) mean line and the NACA 16-series thickness distributions (ref. 4) were used for all blades. These were selected because the resulting flow passages between blades had a streamwise variation of cross-sectional area that was considered desirable; that is, the minimum area or throat occurred between the 5-percent- and 20-percent-chord points and the area increased smoothly from that point to the trailing edge. The large amount of cascade data available for this mean line was also an important consideration.

The maximum thickness of all blade sections was 8 percent of the chord. This was a compromise between the desire for thin sections from choking considerations and for thick sections to permit a wide angle-of-attack range and to provide a rotor-blade root section thick enough to allow a threaded shank fastening to be used.

The blade section cambers and blade setting angles were found directly from the low-speed cascade data of reference 3. The blade cambers are listed as a lift coefficient of isolated airfoils in table I. Four different blades were used in the compressor. Rotors 1, 2, and 3 have blades which are the same except for radial length and setting angle. The same is true for the other groups: rotors 4, 5, and 6;

stators 1, 2, and 3; stators 4, 5, and 6. In each group, the blades were designed for the vector diagrams of the first row and the resulting blade was matched as well as possible to the requirements of the following rows. Solidity was also changed for rotor 3. In table I in the column $\alpha - \alpha_{ISC}$ is shown the amount the design angle of attack differs from the angle of attack selected for a peak free pressure distribution at low speed as published in reference 5. In the column $\alpha - \alpha_{req}$ is shown the difference between the angle of attack at which the blade would produce the desired turning angle and the angle of attack that is available which is determined by the blade twist and the requirements of the other radial stations of the same blade.

The blade chords were about 2 inches for the first three stages in order to keep the Reynolds number above 250,000 for an atmospheric discharge pressure at design conditions. The chord of the last three stages was approximately 1.0 inch.

Mechanical Design

Figure 2 shows the complete six-stage compressor as tested at design blade setting angles. Rotors and stators 1, 2, and 3 were fabricated from 2024T aluminum alloy and rotors and stators 4, 5, and 6 were fabricated from 416 heat-treated stainless steel. All blades were cut on an airfoil duplicating machine and were polished. A turned-shank mounting was used to allow variable blade setting angles. In order to finish-turn the shanks, notches were cut in the blade roots as shown in figure 3. Because of the contour of the inner case, shank size, and chord length, the notches were largest in rotors 1, 2, and 3. They were 6 percent, 7 percent, and 8 percent of the blade span, respectively.

With the high solidity chosen, there was no clearance between the nuts on the rotor-blade shanks if a simple drilled drum was used; also, the stresses would have exceeded a safe margin at 20 percent over speed operation in air. From these considerations, a slotted drum with individual mounting blocks was used. Figure 3 shows a detail of the mounting block and method of holding the last block in place. Using this type of fastening also allowed the solidity to be changed in any of the rotor stages. The outer casing was drilled to mount the stator blades.

Figure 4(a) is a plan view of the test rig; the solid lines indicate the assembly for the air tests and the broken lines, for the Freon tests. The air tests were made with an atmospheric discharge since the cooling capacity of the radiators was not large enough to operate as a closed cycle. An upstream valve in the supply line was used as a throttle for the air tests. The rig was closed for operation in Freon. The system pressure could be varied for the Freon tests. Figure 4(b) is a section

of the compressor. The medium was diffused by a 5.8° conical inner case (the diameter of the inner case varying from 14 to 12 in.) and a radial diffuser. A roller bearing was used in the front, lubricated by an oil mist spray. The rear bearing assembly consisted of a roller bearing carrying the radial load and a Kingsbury type of spherical seated thrust bearing lubricated by a pressurized liquid oil system. After the rotor was assembled, it was balanced as a unit. The blade tip clearance was set at 0.023 to 0.025 inch when cold.

INSTRUMENTATION AND TEST PROCEDURE

In order to measure the overall performance of the compressor, fixed instrumentation was used in the inlet and exit. The approximate axial locations of the instruments were: 3 inches ahead of the first rotor (station 1), 1 inch behind the sixth stator (station 2), and 6.5 inches behind the sixth stator (station 3), as shown in figure 4(b).

Inlet instrumentation (station 1) consisted of: (1) a stagnation-temperature rake located centrally in the annulus and consisting of five double-shielded chromel-alumel thermocouples (fig. 5) equally spaced radially, and (2) four static-pressure orifices on the outer case equally spaced about the circumference.

Exit instrumentation (stations 2 and 3) consisted of: (1) two stagnation-temperature rakes of the same type as used in the inlet located 180° apart and spaced in the center of the annulus, (2) two stagnation-pressure rakes (fig. 5), each consisting of eleven 0.060-inch-diameter tubes, located 180° apart and 90° from the stagnation-temperature rakes and centered in the annulus, and (3) four static-pressure orifices on the outer case equally spaced about the circumference at station 3. For the first three tests, the temperature and pressure rakes were all at station 3, but after the third test one temperature rake and one pressure rake were moved to station 2. This was done to find whether there was a difference in the radial gradient closer to the sixth stator. The circumferential location of the exit instrumentation was determined so that the instrument was in the center of the blade passage. It was assumed that the pressure defects due to the wakes from the sixth stator were negligible as compared with the overall rise through the machine.

Compressor equivalent weight flow was determined from the calibrated venturi meter (fig. 4(a)). The settling-chamber stagnation pressure was measured by two static orifices in the chamber and stagnation temperature, by four shielded thermocouples located in a vertical plane upstream of the inlet. It was assumed that the stagnation pressure in the settling chamber and in the inlet was the same. The outer-casing static pressure was measured along two lines of orifices, 180° apart, located ahead of

each blade row in the same relative position with respect to the blades as shown in figure 6(b).

Five configurations were tested. The first three (configurations A, B, and C) were modifications to obtain the design conditions, and the last two (configurations D and E) were made in an attempt to increase the operating range of the compressor (fig. 6). Table II gives the geometric change, speeds tested, and medium tested in for each configuration. For those tested in Freon, air-equivalent corrected speeds were computed by the method presented in reference 6. Stagnation-pressure rise, stagnation-temperature rise, equivalent weight flow, and shaft torque were measured over a range of mass flows from maximum to unsteady conditions for each speed. An upstream throttle was used for the air tests and the throttle in the rig was used for the Freon tests. Only one configuration, E, was tested in the region of rotating stall and that in air only.

PRESENTATION OF RESULTS

A typical radial distribution of stagnation-pressure ratio and non-dimensional temperature rise at compressor discharge is shown in figure 7. It was found that the numerical average of the pressures was approximately equal to the area-weighted value when the end points were omitted in the numerical average. In this report, numerical averages were used for both the stagnation-pressure ratio and temperature rise.

The overall performance of the several configurations is presented in figures 8 to 15. The following table briefly summarizes the data presented in these figures:

Config-uration	Fig-ure	Medium	Peak efficiency, percent		Percent of mass flow at 100 percent of design speed		
			85 percent of design speed	100 percent of design speed	Maximum flow	P_2/P_1	
						3.0	3.2
A	8	Air	80.0	83.0	96.0	88.0	-----
B	9	Air	79.5	77.5	100.0	100.0	-----
C	10	Air	82.0	82.5	101.5	101.5	101.5
C	11	Freon-12	81.0	81.0	105.0	104.5	104.0
D	12	Air	81.0	82.5	102.5	102.5	102.0
D	13	Freon-12	82.5	80.0	108.0	107.5	107.0
E	14	Air	^a 77.0	^a 77.0	102.0	102.0	102.0
E	15	Freon-12	80.5	82.0	106.0	106.0	105.5

^aEfficiency is based on torque measurements, whereas the others are based on temperature measurements.

DISCUSSION OF RESULTS

The compressor in its design configuration, configuration A, had the flat stagnation-pressure ratio as a function of mass-flow characteristic (fig. 8(a)) that it was designed for but was low in mass flow by 4 percent and had a peak stagnation-pressure ratio of 3.0 as compared with the design value of 3.25. The peak temperature efficiency (fig. 8(b)) at design speed was 83 percent compared with the design adiabatic efficiency of 82.8 percent. The power input was low by about 32 percent; this indicates that the design turning angle was not attained in one or more blade rows. The tip static pressure through the compressor at design speed (fig. 8(c)) was below design values in all rows except the fourth stator. The points used are referenced to the stagnation-pressure-ratio performance curve by Roman numerals. At high mass flows, or open throttle, the sixth stator was choked. At off-design speeds, the static-pressure distribution (fig. 8(c)) had the same stages low, and the sixth stator choked at the high-mass-flow region for speeds as low as 50 percent. Change in speed had little effect on the shape of the static-pressure distribution along the compressor. The flat stagnation-pressure ratio as a function of mass-flow characteristic is limited by the supersonic flow in the sixth stator and the surge or rotating stall at the other end.

In order to reach design conditions, the first rotor and the first, second, third, and fifth stators were staggered as listed in table II to increase the stagnation-pressure ratio and mass flow and, also, to increase the static-pressure rise per row to design values. Configuration B reached design mass flow at a pressure ratio of 3.1 and at an efficiency 7 percent lower than that of configuration A (figs. 9(a) and 9(b)). The overall static-pressure rise was more evenly distributed and closer to design values (fig. 9(c)).

The notches at the root end of the blades of the first three rotors were believed to be partly responsible for the lower-than-design pressure ratio, mass flow, and efficiency. These notches extended radially for 6 percent, 7 percent, and 8 percent of the blade span for rotors 1, 2, and 3, respectively, and possibly caused the flow to separate. This would result in low static-pressure ratio and a low power input. These notches were filled with balsa wood for configuration C.

The performance of configuration C in air is shown in figure 10. Filling the notches raised the mass flow $1\frac{1}{2}$ percent, the peak efficiency 6 percent, and the peak pressure ratio from 3.1 to 3.22 at design speed. Peak efficiency was nearly constant (80 to 82 percent) at all speeds from 30 percent to 100 percent of design speed. The overall tip static-pressure distribution increased to about design at all stages at the low mass flows. The sixth stator again choked at high mass flows.

Configuration C was also tested in Freon-12. Because of the lower ratio of specific heats, the temperature rise in Freon is less than in air for the same pressure ratio. This results in a greater density rise in Freon and, hence, in a greater effective annulus area at the exit of the machine. Appendix B shows that for this compressor the density rise is effectively 24 percent greater in Freon than in air. The increase in density produces an increase in weight flow. Because of the higher weight flows and lower sonic velocities, the blade rows will operate at a higher angle of attack which is progressively increasing from inlet to exit, causing stall at a higher weight flow, and limiting the overall range at any one speed.

Figure 11 shows the performance of configuration C in Freon-12. The peak temperature efficiency and stagnation-pressure ratio are approximately the same as in air, but the mass flow increased about 5 percent. Figure 11(a) shows the decrease in range from the air tests (fig. 10(a)) at the higher speeds. The static-pressure rise at near stall was approximately the same as air, but at the open throttle position it fell in the midstages (fig. 11(c)). The higher mass flows and mismatch could account for this drop in static-pressure rise in the middle of the compressor. The sixth stator passage shows supersonic choking as low as 85 percent of design speed at the high mass flows, as was found in air. After tests of configuration C were completed, the instrumentation was changed to one stagnation-temperature rake and one stagnation-pressure rake at station 2 and one set at station 3. The results for configurations D and E are from the instrumentation at station 2.

For configuration D, rotors 1, 2, 5, and 6 were restaggered to increase the power input in the first two stages and to decrease it in the last stages in an attempt to increase the weight-flow operating range. The performance data for configuration D in air are shown in figure 12. The range was the same as for configuration C and there was little or no effect on the performance. At the high values of mass flow, the flow behind the sixth stator is supersonic. At some speeds, the instruments at station 2 indicate no change in pressure ratio at the maximum flow possibly because of the supersonic flow.

Configuration D was also tested in Freon-12 (fig. 13). The peak stagnation-pressure ratio and temperature efficiencies were the same, but the mass flow was 5 percent higher in Freon. For 100 percent of design speed and above, the range of weight-flow variation decreased appreciably in Freon as was noted in configuration C. The static-pressure distribution was the same as the distribution found for configuration C in Freon.

The solidity of rotor 1 was lowered for configuration E in an attempt to increase the weight-flow operating range. The lower solidity rotor should have a greater variation in deviation angle and, hence, should delay stall of the last stages until lower weight flows are reached. The

performance of configuration E (fig. 14) showed that the range, peak stagnation-pressure ratio, and static-pressure distribution were the same as those for configuration D in air (fig. 12). For this test, torque efficiency is presented since the temperature readings were in error. The peak torque efficiency presented (fig. 14(b)) is about 4 percent to 5 percent lower compared with the temperature efficiencies presented for previous tests. For tests where both the temperature and torque readings were available, the torque efficiencies were approximately 4 percent lower. This would indicate then that there was no change in the efficiency of the compressor due to the lower solidity. This lower value can be partially attributed to the two ball bearings, three roller bearings, one thrust bearing, and three carbon seals after the torque coupling.

At the lower speeds, the compressor was operated in the rotating stall range. Previous tests were made with the unsteady flow as a limit. Above 75 percent of design speed, the unsteady flow was the surge limit. The torque efficiencies are indicated in figure 14(b) by dashed lines.

The compressor design had a possible application for air removal from a wind tunnel which was to operate at varying amounts of moisture content. At design speed, water was injected in the airstream to find the effect of moisture on this compressor. Four nozzles were used, equally spaced 22 inches ahead of the first blade row and aligned to spray toward the center of the annulus. Water was sprayed in at rates up to 1.5 percent of the weight flow with no change in the torque efficiency or weight flow. The solid points in figure 14 indicate the data when water was injected. Temperature readings were not taken since there was some question whether all the water evaporated. The outer casing behind the sixth stator was cooled to 55 percent of its initial temperature rise with the maximum flow of water.

Configuration E was also tested in Freon-12 (fig. 15). The effect of operating in Freon-12 was the same as in other Freon tests. The mass flow increased approximately 5 percent; the overall weight-flow range decreased at design speed and above. The peak values of pressure ratio and temperature efficiency were the same as in air. The static-pressure distribution again showed the same characteristic as was found with configurations C and D in Freon.

Figures 6(a) and 6(b) show the compressor after configuration E was tested. The lower solidity first rotor and lines of boundary flow can be seen.

CONCLUSIONS

A six-stage axial-flow compressor with a tip speed of 550 feet per second and a flat operating characteristic at constant speed was designed for a specific weight flow of 21.3 pounds per second per square foot of frontal area at atmospheric discharge with a pressure ratio of 3.25 and a hub-tip radius ratio of 0.7. All stages turned axially and were symmetrical at the pitch section. The blade cambers and setting angles were selected from low-speed cascade data. The compressor had a possible immediate application to air removal from a slotted-throat wind tunnel, but the design theory would apply to any low-speed industrial compressor or second spool of a turbojet engine. The following conclusions were obtained from the test results:

1. A flat pressure ratio as a function of weight flow over a range of 10 percent of design flow at constant speed was obtained by making the rotational speed equal to the change in tangential velocity through the rotor at the mean radius with the limit of weight flow caused by choking in the sixth stator.

2. The design value of average stagnation-pressure ratio of 1.22 per stage was obtained at a tip speed of 550 feet per second by using an axial velocity of 650 feet per second. The usual limits of static-pressure rise divided by entering impact pressures were not exceeded.

3. Peak efficiency was nearly constant (80 to 82 percent) at all speeds from 30 percent to 100 percent of design speed for the configuration which met design conditions.

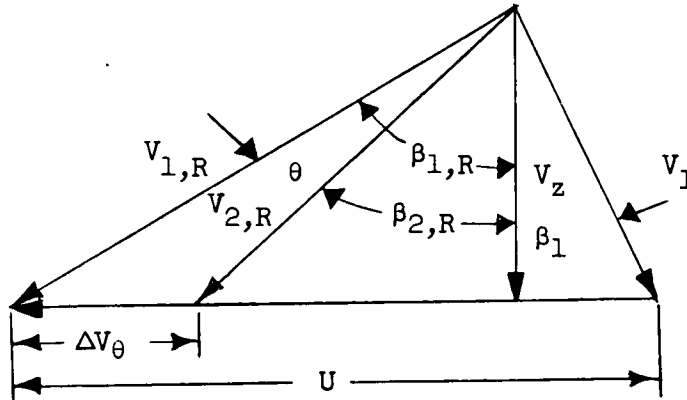
Langley Aeronautical Laboratory,
National Advisory Committee for Aeronautics,
Langley Field, Va., December 2, 1957.

APPENDIX A

DERIVATION OF AN EQUATION FOR THE RATE OF CHANGE OF WORK

INPUT WITH A CHANGE IN AXIAL VELOCITY

A typical velocity diagram is shown in sketch 1:



Sketch 1

It is assumed that:

1. Entering and leaving axial velocities are equal.
2. Streamlines remain at the same radii.
3. Leaving flow direction relative to the rotor remains constant as entering direction varies.

The work input per unit mass flow is $U \Delta V_\theta$. The change in tangential velocity is

$$\Delta V_\theta = V_{\theta,1,R} - V_{\theta,2,R} \quad (A1)$$

or

$$\Delta V_\theta = U - V_z \tan \beta_1 - V_z \tan \beta_{2,R} \quad (A2)$$

Differentiating the change in tangential velocity with respect to the axial velocity gives

$$\frac{d(\Delta V_\theta)}{dV_z} = -(\tan \beta_1 + \tan \beta_{2,R}) \quad (A3)$$

and multiplying both sides of equation (3) by $V_z/\Delta V_\theta$ gives

$$\frac{\frac{d(\Delta V_\theta)}{\Delta V_\theta}}{\frac{dV_z}{V_z}} = \frac{-(V_z \tan \beta_1 + V_z \tan \beta_{2,R})}{\Delta V_\theta} \quad (A4)$$

Simplifying equation (4) by use of equation (2) gives

$$\frac{\frac{d(\Delta V_\theta)}{\Delta V_\theta}}{\frac{dV_z}{V_z}} = \frac{\Delta V_\theta - U}{\Delta V_\theta} \quad (A5)$$

or

$$\frac{\frac{d(\Delta V_\theta)}{\Delta V_\theta}}{\frac{dV_z}{V_z}} = 1 - \frac{U}{\Delta V_\theta} \quad (A6)$$

Equation (6) is an equation for the rate of change of work input with a change in axial velocity at a constant rotational speed.

APPENDIX B

EFFECT OF TESTING IN FREON-12

The work input is

$$c_p \Delta T = U \Delta V_\theta \quad (B1)$$

and the isentropic relations for a perfect gas are

$$\frac{P_2}{P_1} = \left(\frac{T_2}{T_1} \right)^{\gamma/(\gamma-1)} = \left(\frac{\rho_2}{\rho_1} \right)^\gamma \quad (B2)$$

For a polytropic process, equation (2) becomes

$$\frac{P_2}{P_1} = \left(\frac{T_2}{T_1} \right)^{n/(n-1)} = \left(\frac{\rho_2}{\rho_1} \right)^n \quad (B3)$$

Combining equations (1) and (3) results in

$$\frac{P_2}{P_1} = \left(\frac{U \Delta V_\theta}{c_p T_1} + 1 \right)^{n/(n-1)} \quad (B4a)$$

$$\frac{\rho_2}{\rho_1} = \left(\frac{U \Delta V_\theta}{c_p T_1} + 1 \right)^{n/(n-1)} \quad (B4b)$$

The ratio of pressure ratio and density ratio of air to Freon-12 can be written as

$$\frac{\left(\frac{P_2}{P_1} \right)_{\text{air}}}{\left(\frac{P_2}{P_1} \right)_{\text{Freon-12}}} = \frac{\left(\frac{U \Delta V_\theta}{c_p T_1} + 1 \right)_{\text{air}}^{n/(n-1)}}{\left(\frac{U \Delta V_\theta}{c_p T_1} + 1 \right)_{\text{Freon-12}}^{n/(n-1)}} \quad (B5a)$$

$$\frac{\left(\frac{\rho_2}{\rho_1}\right)_{\text{Freon-12}}}{\left(\frac{\rho_2}{\rho_1}\right)_{\text{air}}} = \frac{\left(\frac{P_2}{P_1}\right)_{\text{Freon-12}}^{1/n}}{\left(\frac{P_2}{P_1}\right)_{\text{air}}^{1/n}} \quad (\text{B5b})$$

The ratio of the tip speeds for the same relative inlet Mach number in air and in Freon-12, assuming no inlet whirl, is from reference 6

$$\frac{U_{\text{air}}}{U_{\text{Freon-12}}} = \left\{ \frac{\left[\frac{\gamma R}{2 + (\gamma - 1)M_1^2} \right]_{\text{air}}}{\left[\frac{\gamma R}{2 + (\gamma - 1)M_1^2} \right]_{\text{Freon-12}}} \right\}^{1/2} \quad (\text{B6})$$

where R in this equation is the universal gas constant.

For a multistage compressor with a symmetrical vector diagram where all stages turn axially and the work input is constant per stage regardless of the output of the previous stage, the foregoing equations can be used. The overall stagnation-pressure ratio can be computed without a stage-by-stage analysis since $U = \Delta V_0$. If a polytropic efficiency of 85.8 percent and an inlet absolute Mach number of 0.6 are assumed, equation (B5a) can be evaluated for the design conditions of the subject compressor. The resulting ratio is

$$\frac{\left(\frac{P_4}{P_1}\right)_{\text{air}}}{\left(\frac{P_4}{P_1}\right)_{\text{Freon-12}}} = \frac{\left(\frac{U^2}{c_p T_1} + 1\right)^{3.0}}{\left(\frac{U^2}{c_p T_1} + 1\right)^{7.7}} = 1.025 \quad (\text{B7})$$

This result indicates that the pressure ratio should be 2.5 percent less in Freon-12 for design efficiency. For an air design pressure ratio of 3.25, from equation (B5b) the resulting ratio is

$$\frac{\left(\frac{\rho_4}{\rho_1}\right)_{\text{Freon-12}}}{\left(\frac{\rho_4}{\rho_1}\right)_{\text{air}}} = \frac{\left(\frac{P_4}{P_1}\right)_{\text{Freon-12}}^{0.870}}{\left(\frac{P_4}{P_1}\right)_{\text{air}}^{0.667}} = 1.243 \quad (\text{B8})$$

REFERENCES

1. Erwin, John R., and Schulze, Wallace M.: Investigation of an Impulse Axial-Flow Compressor. NACA RM L9J05a, 1950.
2. Schulze, Wallace M., Erwin, John R., and Westphal, Willard R.: Investigation of an Impulse Axial-Flow Compressor Rotor Over a Range of Blade Angles. NACA RM L50F27a, 1950.
3. Savage, Melvyn: Analysis of Aerodynamic Blade-Loading-Limit Parameters for NACA 65- $(C_{l_0} A_{10})_{10}$ Compressor-Blade Sections at Low Speeds. NACA RM L54L02a, 1955.
4. Abbott, Ira H., Von Doenhoff, Albert E., and Stivers, Louis S., Jr.: Summary of Airfoil Data. NACA Rep. 824, 1945. (Supersedes NACA WR L-560.)
5. Felix, A. Richard: Summary of 65-Series Compressor-Blade Low-Speed Cascade Data by Use of the Carpet-Plotting Technique. NACA TN 3913, 1957. (Supersedes NACA RM L54H18a.)
6. Boxer, Emanuel, and Erwin, John R.: Investigation of a Shrouded and an Unshrouded Axial-Flow Supersonic Compressor. NACA RM L50G05, 1950.

TABLE I.- DESIGN VALUES FOR TEST COMPRESSOR

Blade row	Radius	M	V_z , ft/sec	V_θ , ft/sec	β , deg	θ , deg	σ	Chord	C_{l_0}	α , deg	$\beta - \alpha$, deg	$\alpha - \alpha_{LSC}$, deg	$\alpha - \alpha_{req}$, deg
R1	0.667	0.786	650	550.7	40.3	28.9	1.30	2.178	1.40	18.1	22.2	2.1	0
	.582	.746		481.0	36.5	36.5	1.42	2.089	1.70	21.6	14.9	2.1	0
	.498	.710		411.3	32.3	45.4	1.60	2.000	2.00	25.4	6.9	2.1	0
S1	.667	.689	650	420.1	32.9	32.9	1.40	2.345	1.61	18.4	14.5	0	0
	.582	.720		481.0	36.5	36.5	1.48	2.172	1.78	20.5	16.0	0	0
	.498	.765		562.5	40.9	40.9	1.60	2.000	1.98	23.2	17.7	0	0
R2	.667	.759	650	550.7	40.3	30.5	1.28	2.140	1.52	18.6	21.7	1.4	-.5
	.595	.726		491.3	37.1	37.1	1.38	2.064	1.78	21.7	15.4	1.9	0
	.523	.695		431.9	33.6	44.6	1.51	1.988	2.04	25.1	8.5	2.0	-.8
S2	.667	.674	650	438.3	34.0	34.0	1.40	2.345	1.61	19.5	14.5	1.1	-.1
	.695	.701		491.3	37.1	37.1	1.47	2.198	1.73	21.3	15.8	1.3	-.2
	.523	.737		558.8	40.7	40.7	1.56	2.051	1.91	23.4	17.3	1.2	0
R3	.667	.733	650	550.7	40.3	31.8	1.35	2.116	1.60	18.8	21.5	1.6	.8
	.605	.705		499.6	37.6	37.6	1.44	2.051	1.83	21.6	16.0	1.8	.8
	.543	.679		448.6	34.6	44.0	1.55	1.983	2.05	24.5	10.1	1.4	1.0
S3	.667	.659	650	453.3	34.9	34.9	1.40	2.345	1.61	20.4	14.5	2.0	-.4
	.605	.682		499.6	37.6	37.6	1.46	2.219	1.72	22.0	15.6	2.0	-.4
	.543	.712		556.5	40.6	40.6	1.53	2.092	1.86	23.8	16.8	2.2	0
R4	.667	.709	650	550.7	40.3	32.8	1.34	1.007	1.59	20.0	20.3	2.1	0
	.613	.685		506.4	37.9	37.9	1.46	1.007	1.75	22.2	15.7	2.1	0
	.560	.663		462.2	35.4	43.5	1.60	1.007	1.91	24.6	10.8	2.1	0
S4	.667	.644	650	465.7	35.6	35.6	1.34	1.023	1.83	19.9	15.7	0	0
	.613	.664		506.4	37.9	37.9	1.46	1.023	1.88	21.3	16.6	0	0
	.560	.688		554.9	40.5	40.5	1.60	1.023	1.93	22.7	17.8	0	0
R5	.667	.686	650	550.7	40.3	33.7	1.34	1.007	1.63	20.6	19.7	2.3	0
	.620	.666		512.0	38.2	38.2	1.44	1.007	1.77	22.6	15.6	2.4	0
	.573	.648		473.3	36.1	43.1	1.56	1.007	1.91	24.8	11.3	2.5	-.3
S5	.667	.629	650	476.0	36.2	36.2	1.34	1.023	1.83	20.5	15.7	.6	.1
	.620	.646		512.0	38.2	38.2	1.44	1.023	1.87	21.7	16.5	.5	-.2
	.573	.667		553.8	40.4	40.4	1.56	1.023	1.92	22.9	17.5	.6	-.1
R6	.667	.665	650	550.7	40.3	34.5	1.34	1.007	1.66	21.4	18.9	2.9	.5
	.626	.648		516.6	38.5	38.5	1.43	1.007	1.79	23.2	15.3	2.9	-.2
	.584	.632		482.6	36.6	42.8	1.53	1.007	1.91	25.1	11.5	3.1	0
S6	.667	.615	650	484.7	36.7	36.7	1.34	1.023	1.83	21.0	15.7	1.1	-.1
	.626	.629		516.6	38.5	38.5	1.43	1.023	1.87	22.1	16.4	1.1	-.1
	.584	.647		553.1	40.4	40.4	1.53	1.023	1.91	23.2	17.2	1.3	0

TABLE II.- SUMMARY OF CONFIGURATIONS TESTED

Config- uration	Description	Test medium	Speeds tested, (percent of design)
A	Original blade setting angle	Air	40, 50, 60, 75, 80, 85, 95, 100, 105
B	Blade setting angles changed by the following amounts to raise angle of attack from that of configuration A: <div style="display: flex; justify-content: space-around;"> <div>R1 2° S1 4° R2 0° S2 5°</div> <div>R3 0° S3 5° R4 0° S4 0°</div> <div>R5 0° S5 5° R6 0° S6 0°</div> </div>	Air	60, 75, 80, 85, 95, 100, 105, 110
C	Same configuration as B except notches in R1, R2, and R3 were filled with balsa.	Air Freon-12	40, 60, 75, 80, 85, 95, 100 50, 60, 80, 85, 90, 95, 100, 105, 110, 115
D	Blade setting angles changed by the following amounts to raise angle of attack from that of configura- tion A: <div style="display: flex; justify-content: space-around;"> <div>R1 5° S1 4° R2 2° S2 5°</div> <div>R3 0° S3 5° R4 0° S4 0°</div> <div>R5 -2° S5 5° R6 -2° S6 0°</div> </div>	Air Freon-12	60, 75, 80, 85, 95, 100, 105 60, 75, 85, 95, 100, 105
E	Same blade setting angles as configuration D. Five blades removed from the first rotor.	Air Freon-12	30, 40, 50, 60, 75, 80, 85, 95, 100, 105, 110 30, 40, 50, 60, 75, 80, 85, 90, 95, 100, 105, 110

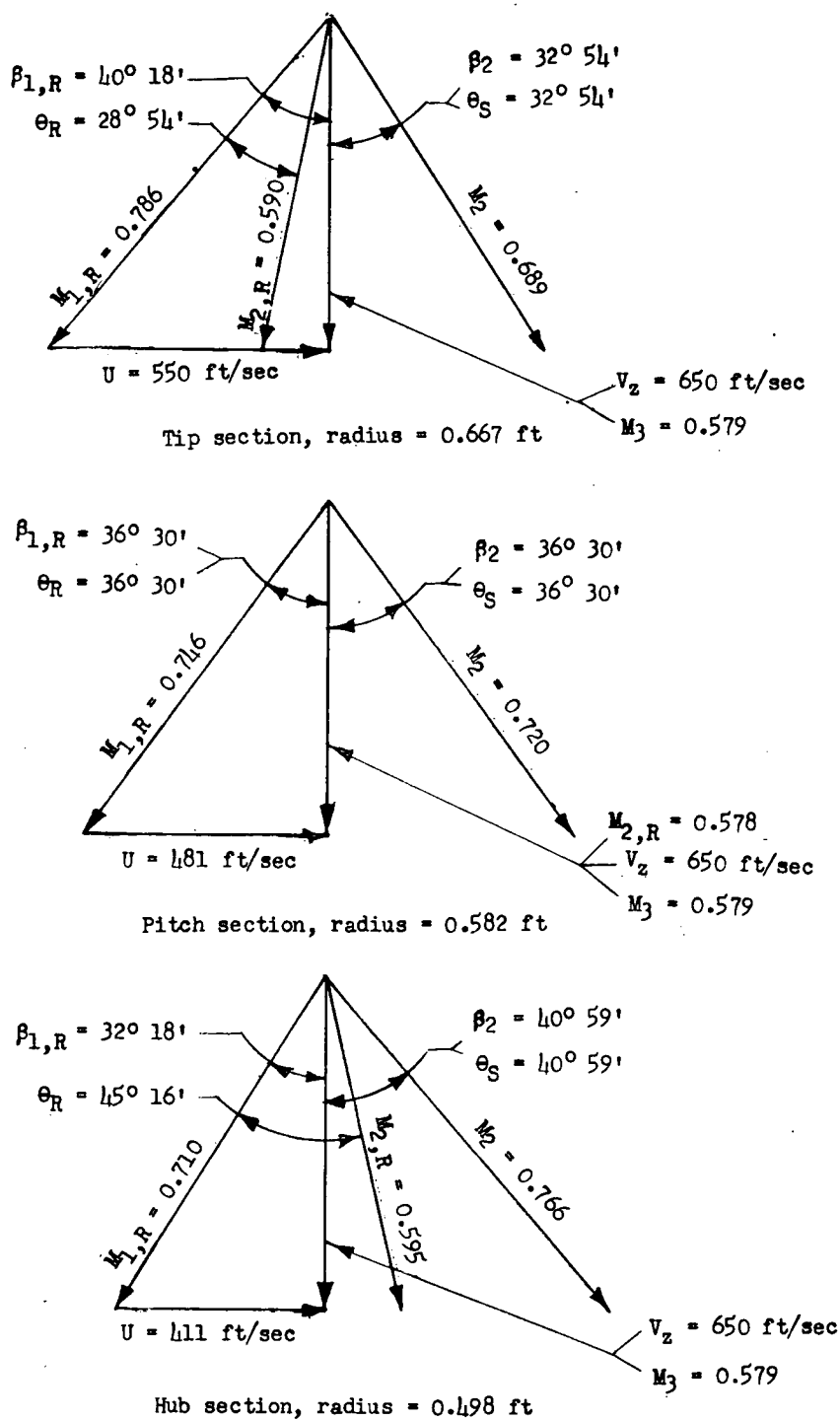
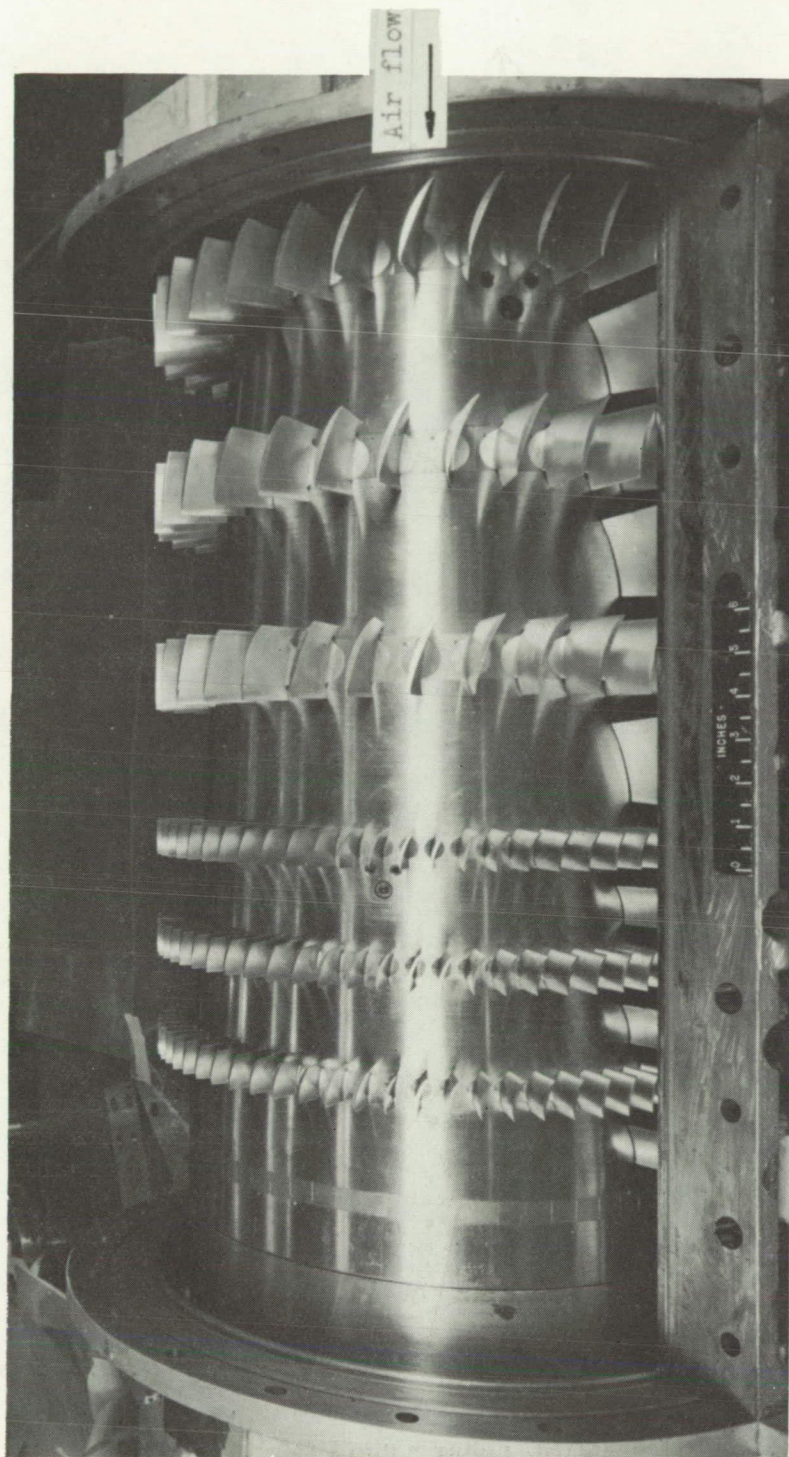
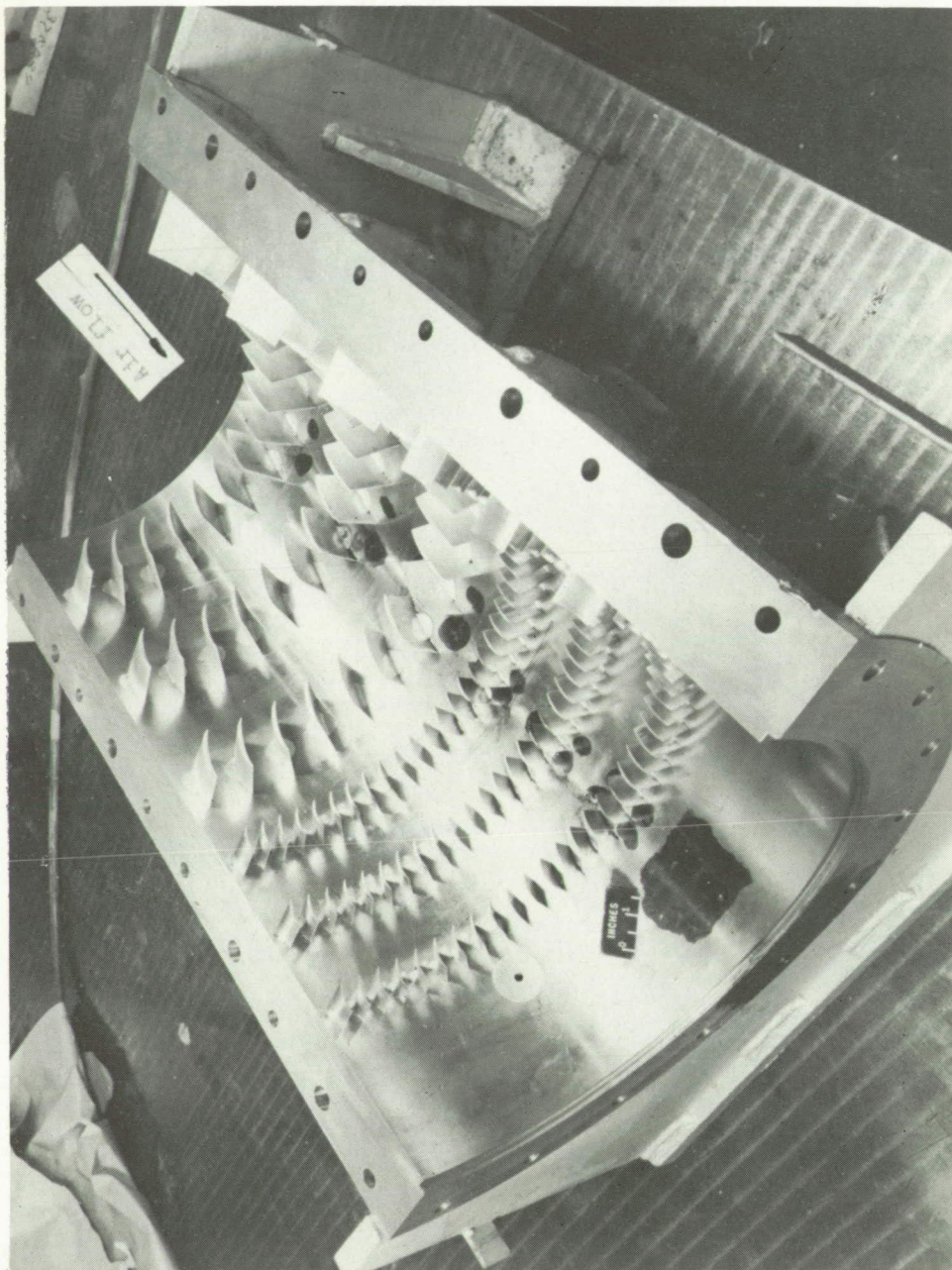


Figure 1.- Design vector diagram for first stage of six-stage compressor at several radii.



(a) Rotor assembly. L-93975.1
Figure 2.- Six-stage compressor assembly. Configuration A.



L-93972.1

(b) Stator assembly.

Figure 2.- Concluded.

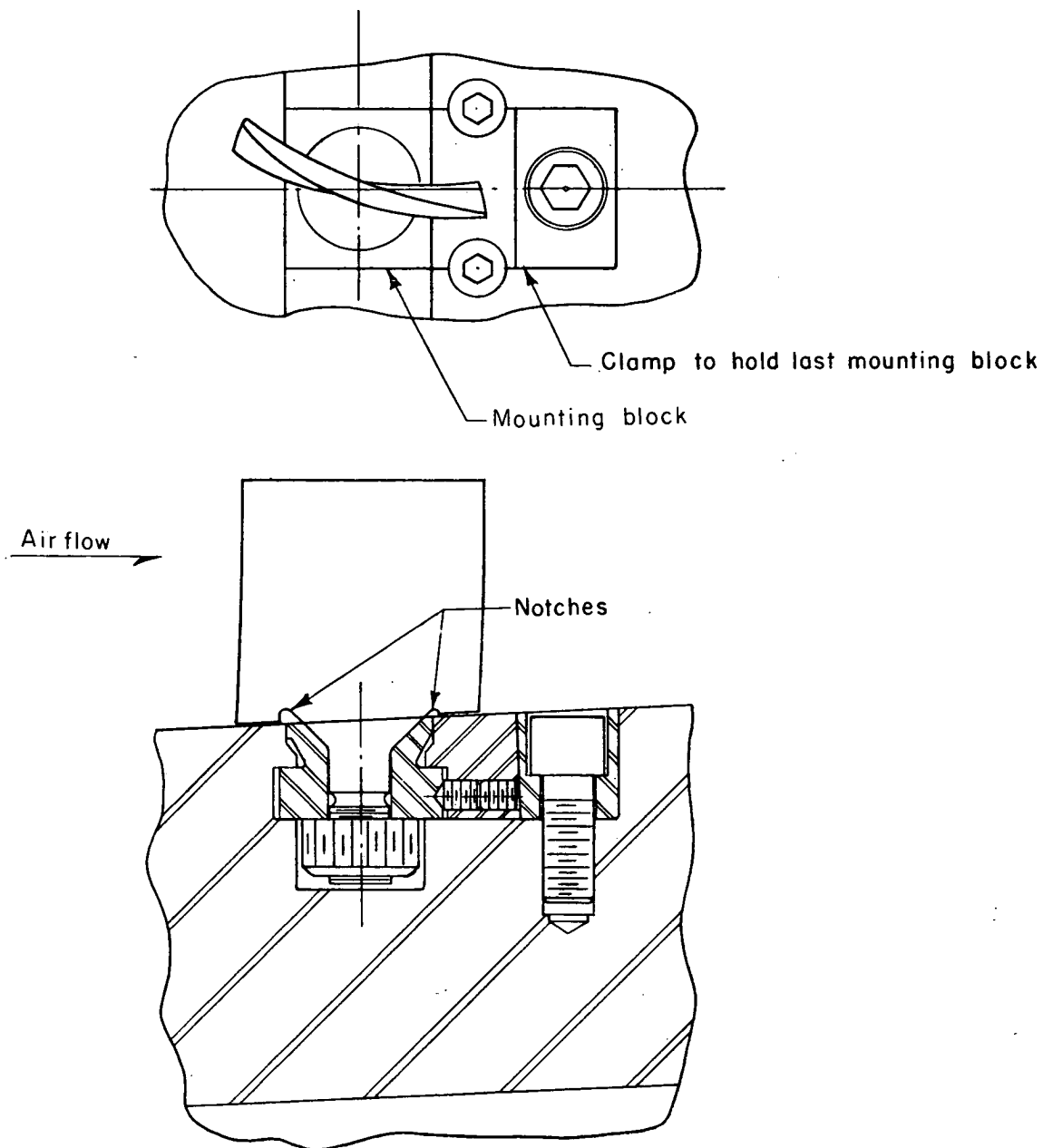
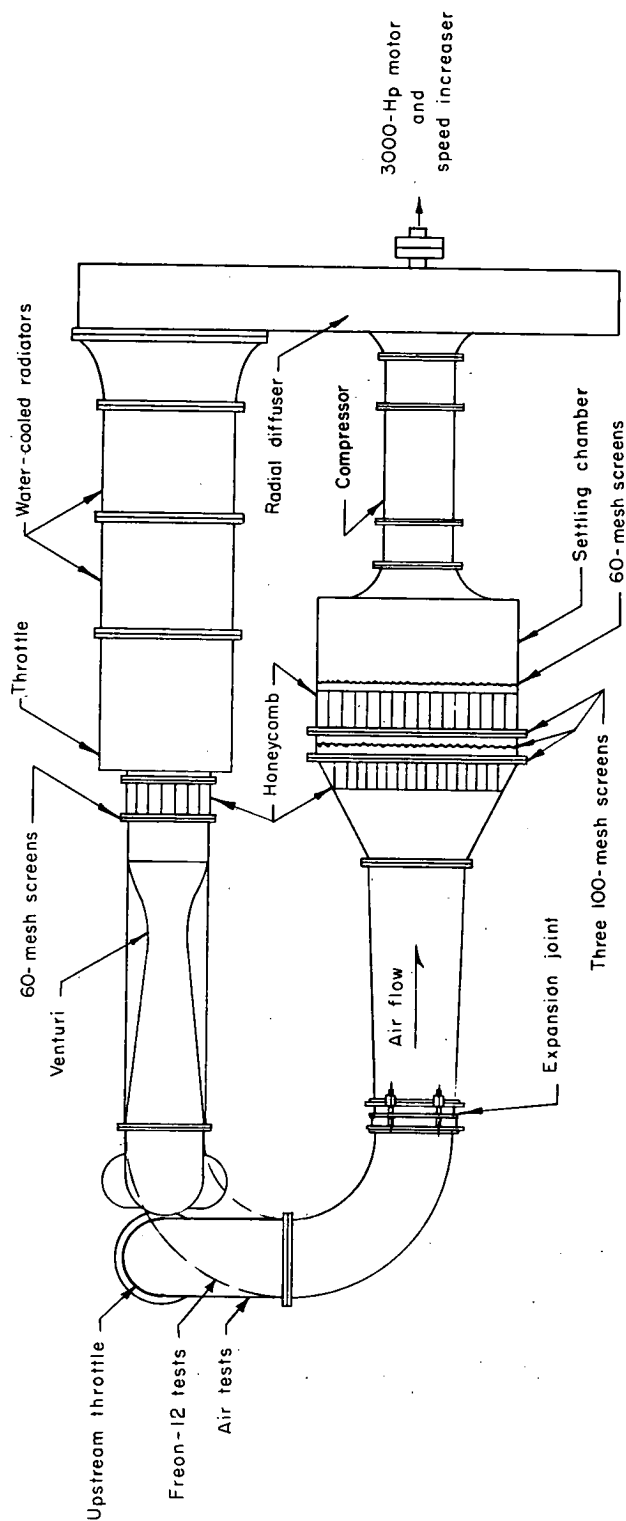
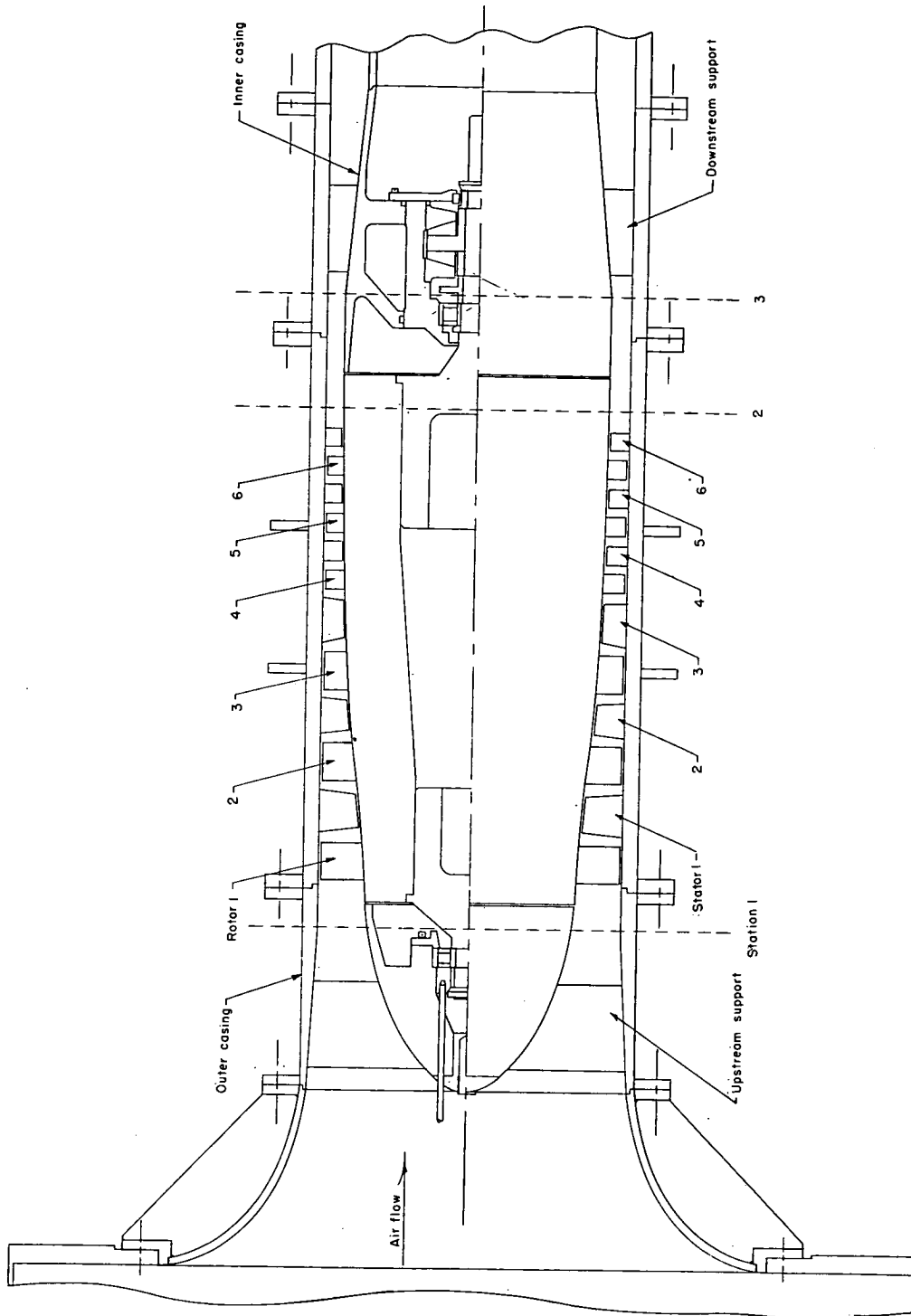


Figure 3.- Detail of blade mounting and notches in blade.



(a) Plan view of loop.

Figure 4.- Schematic diagram of compressor test installation.



(b) Compressor details.

Figure 4.- Concluded.

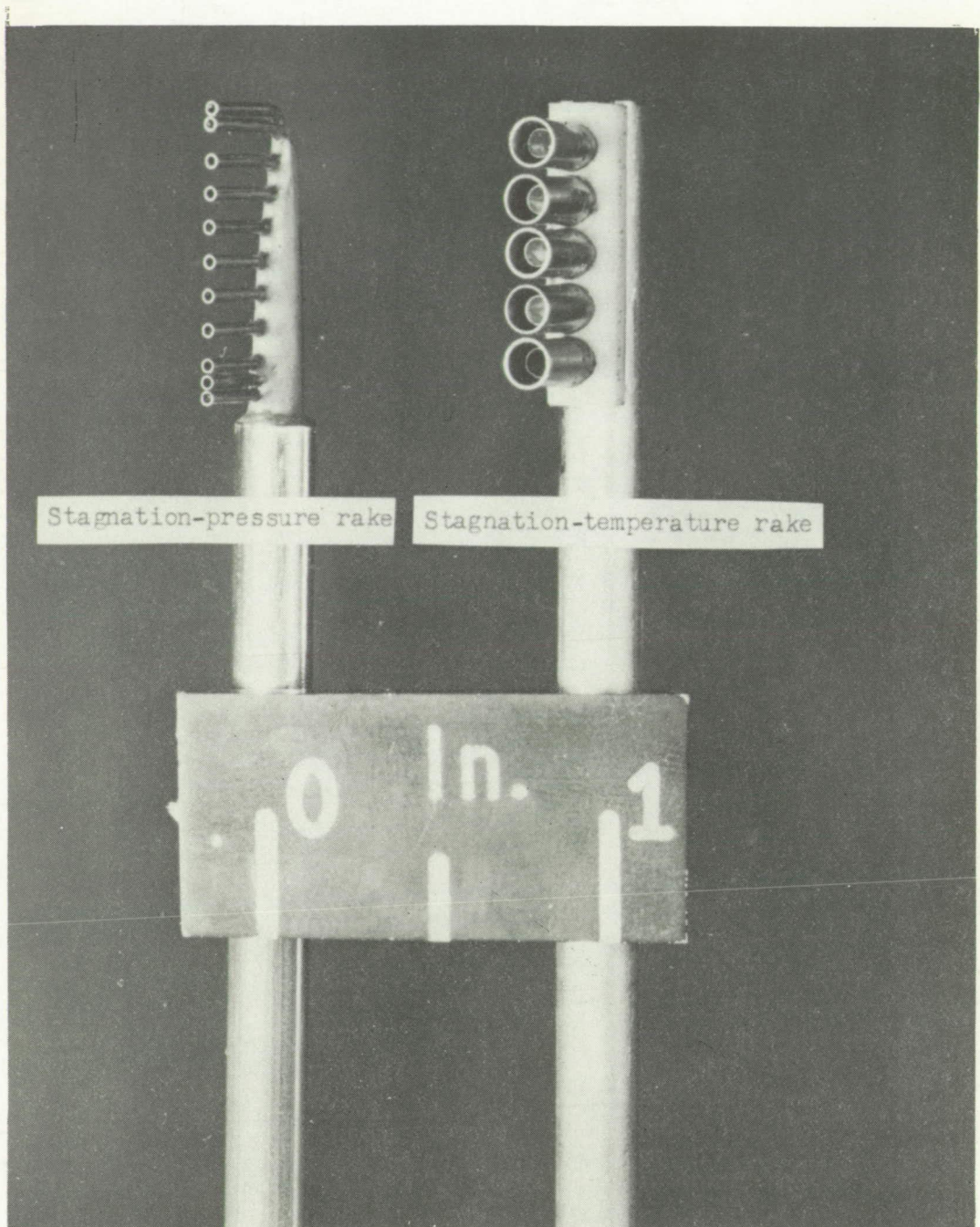
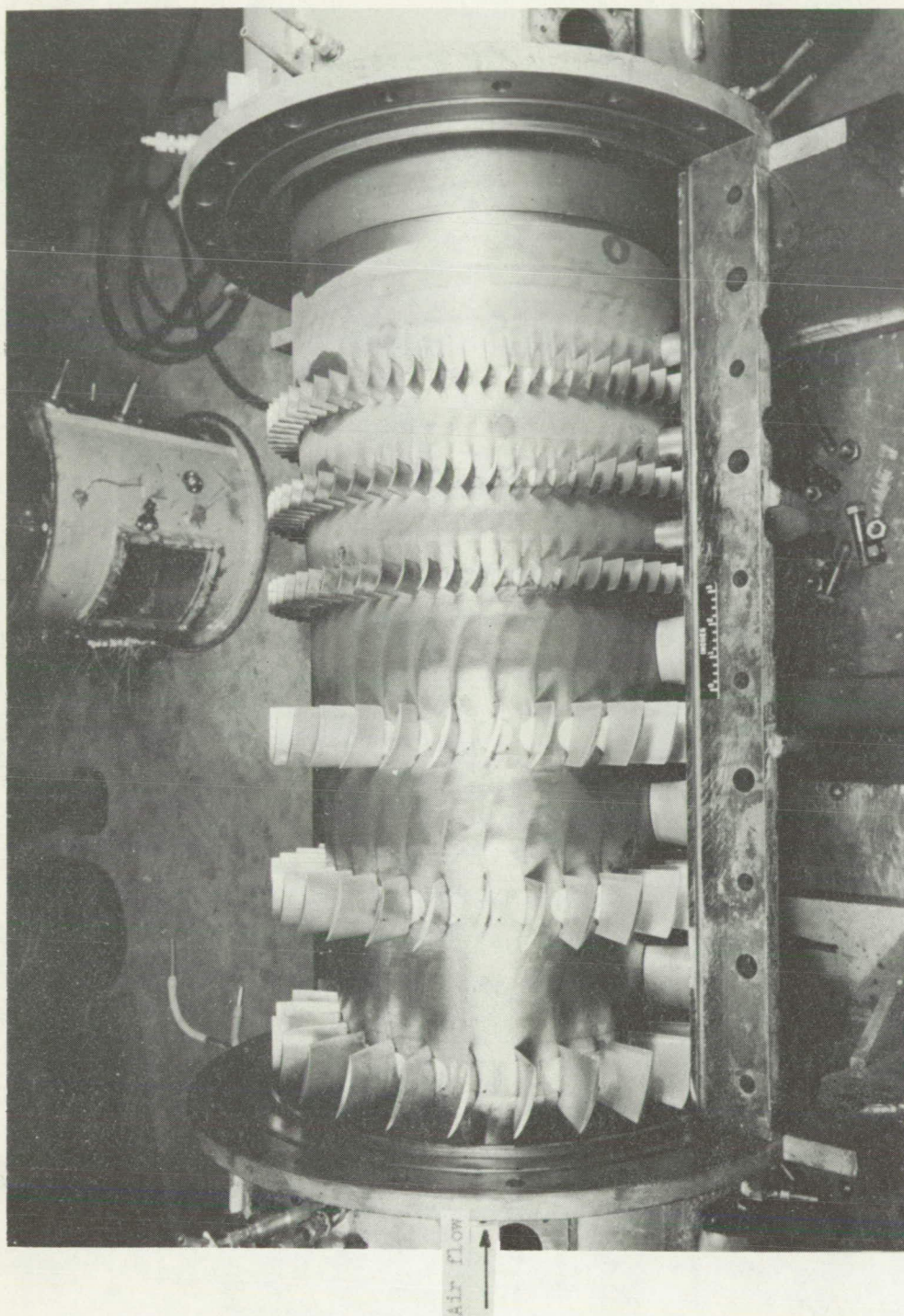


Figure 5.- Instruments.

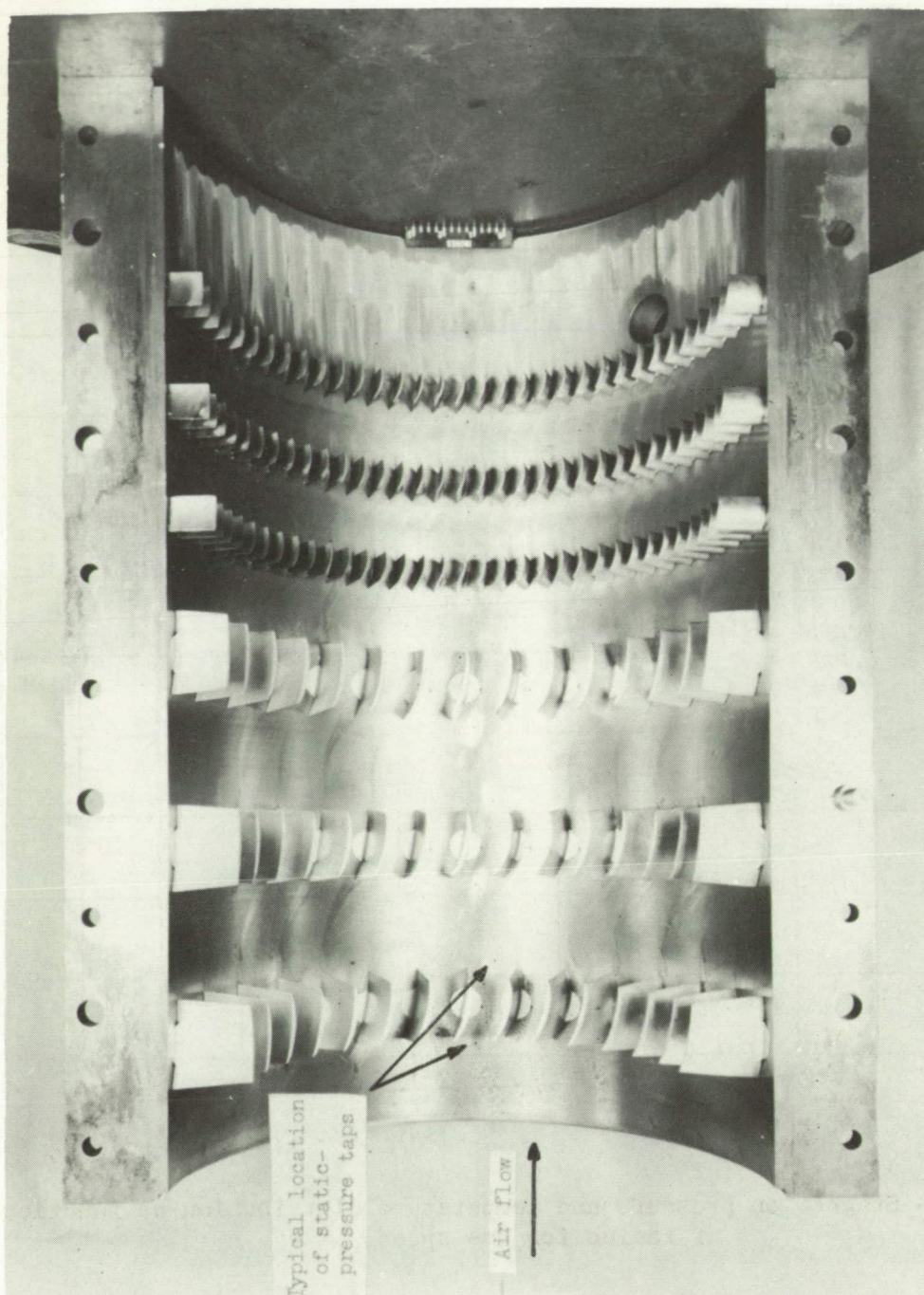
L-57-2230.1



(a) Rotor assembly.

L-96063.1

Figure 6.- Six-stage compressor assembly after solidity change. Configuration E.



(b) Stator assembly.

L-96064.1

Figure 6.- Concluded.

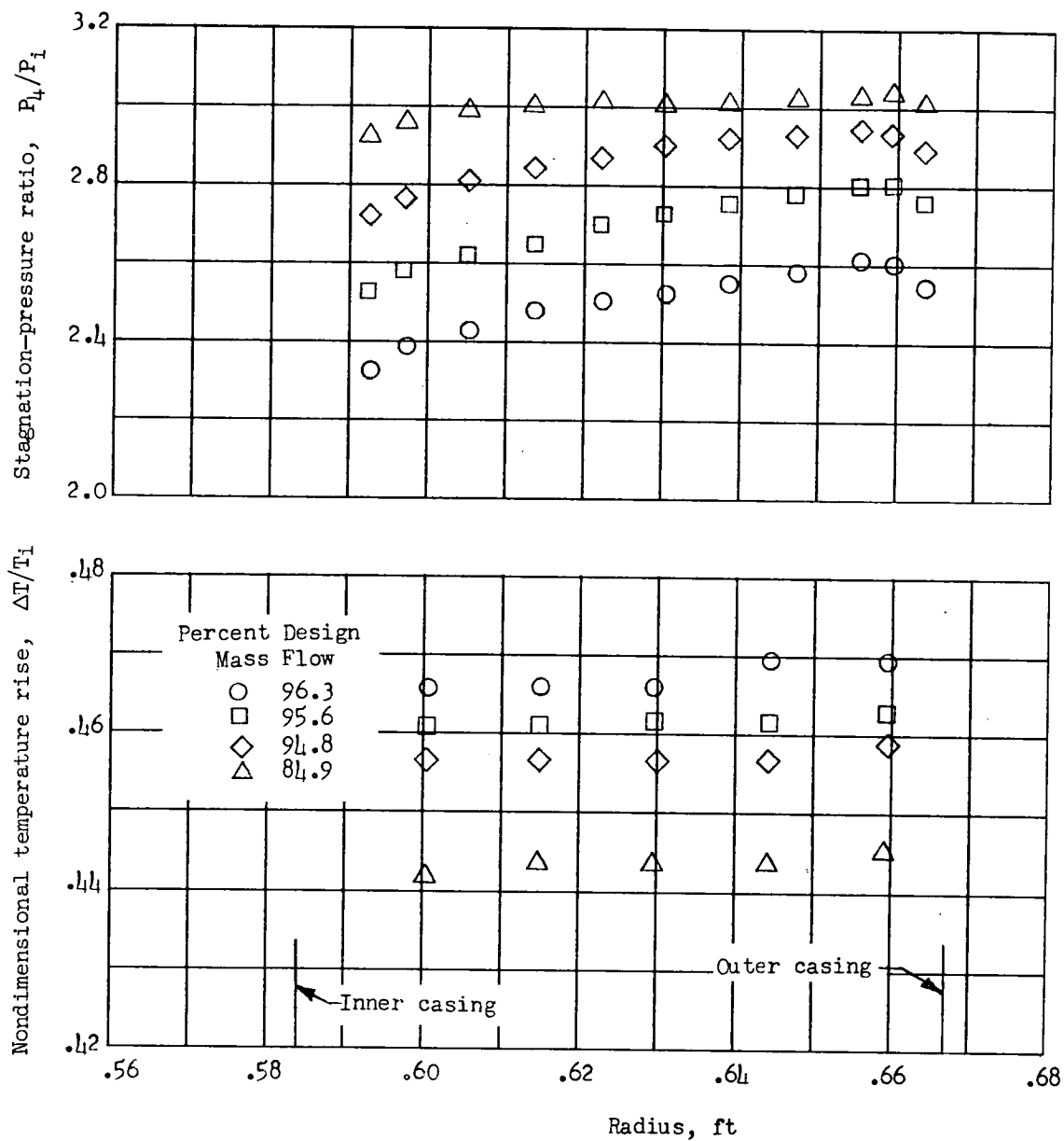
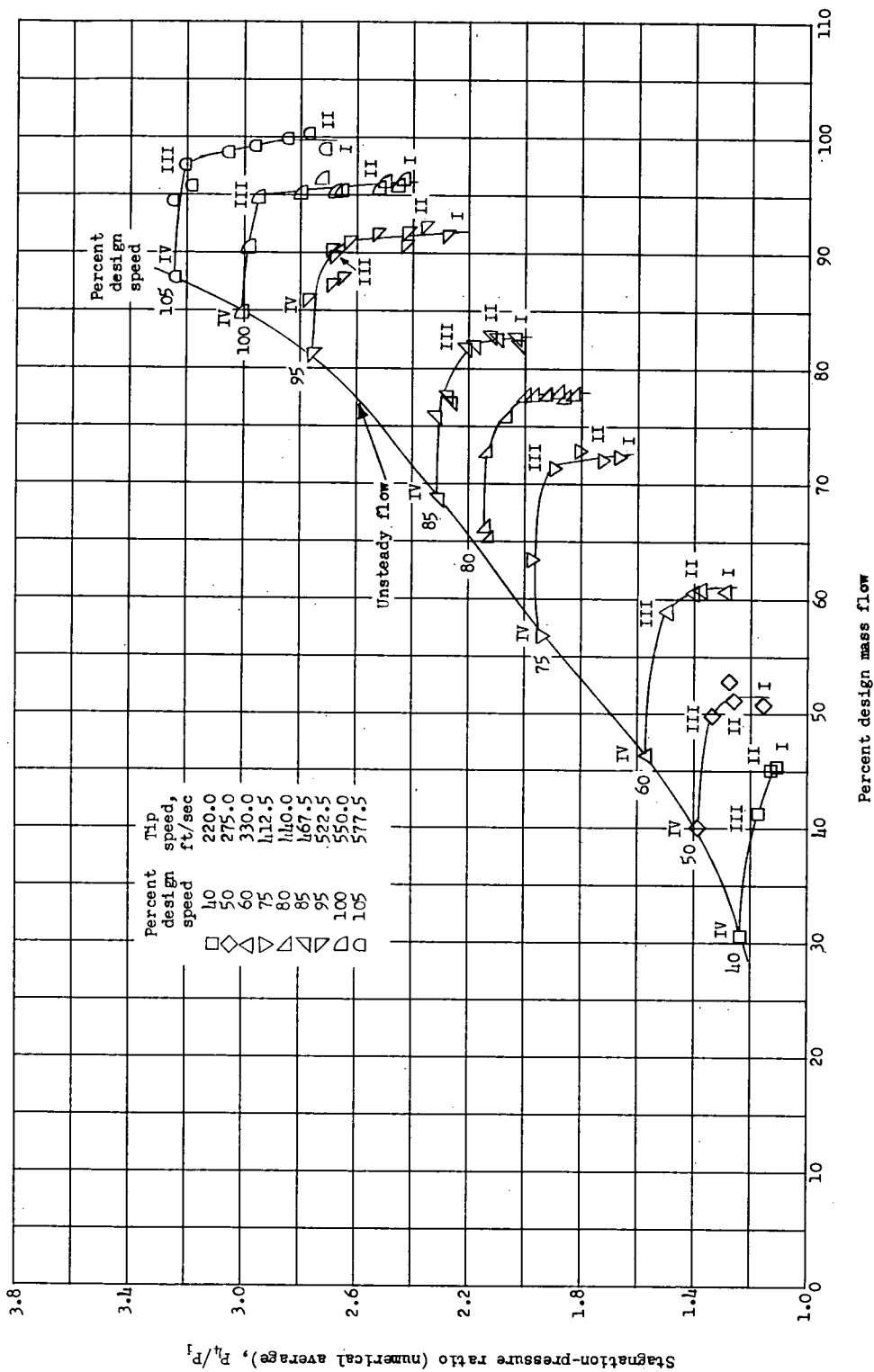
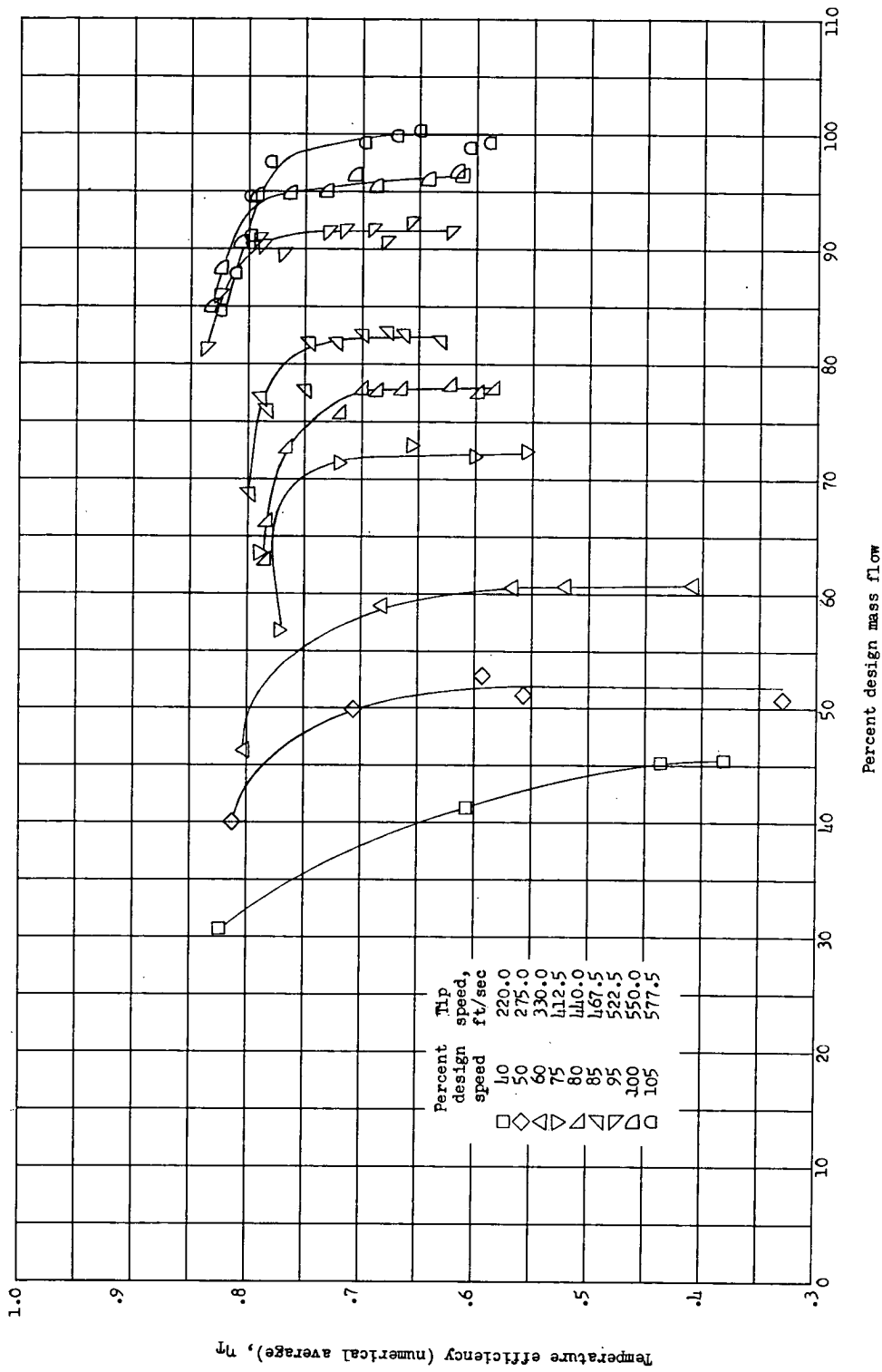


Figure 7.- Stagnation pressure and temperature distribution as functions of radius for one speed.

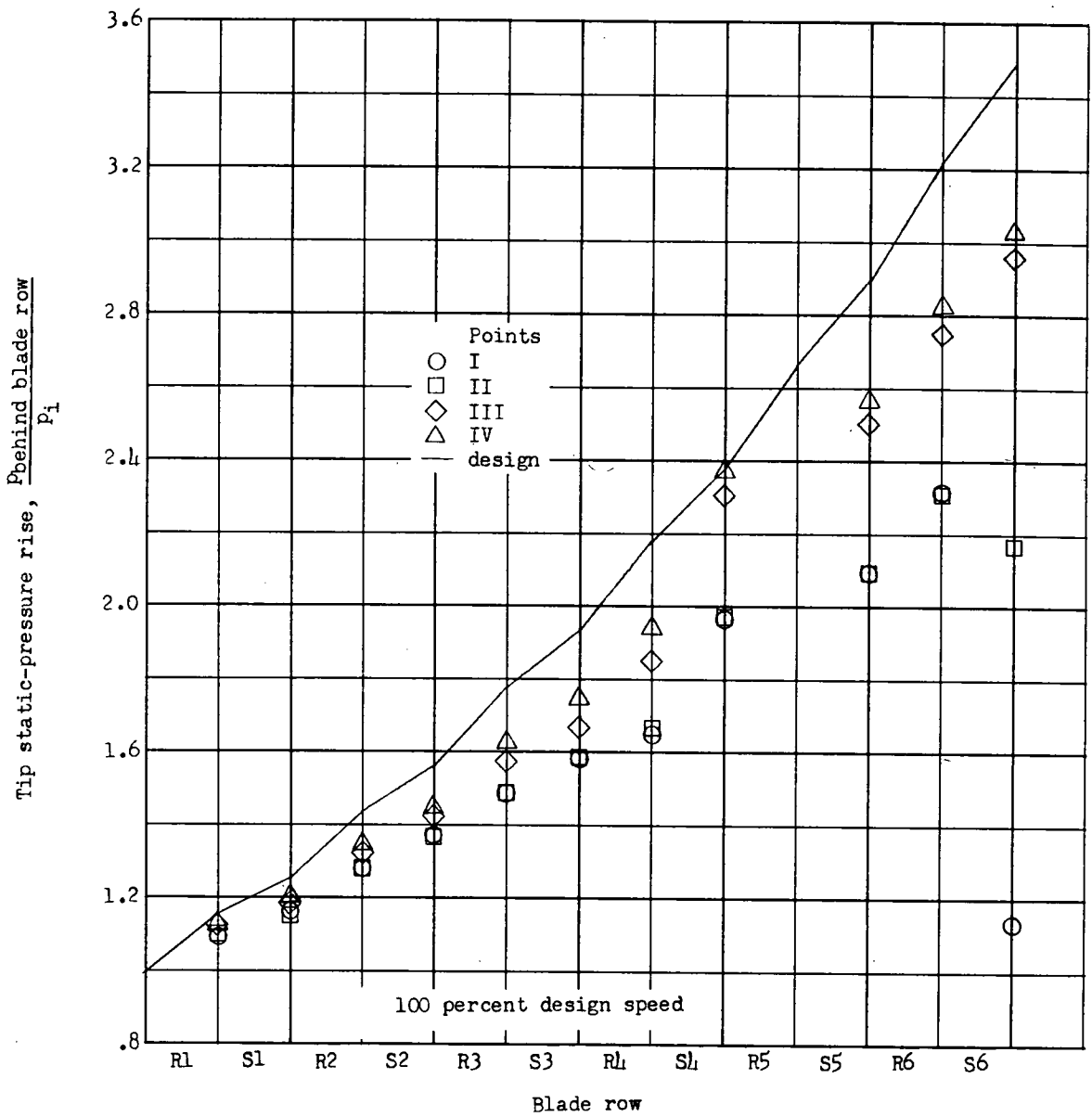


(a) Stagnation-pressure ratio (numerical average) as a function of percent design mass flow.
 Figure 8.- Overall performance of a six-stage axial-flow compressor in air. Configuration A.



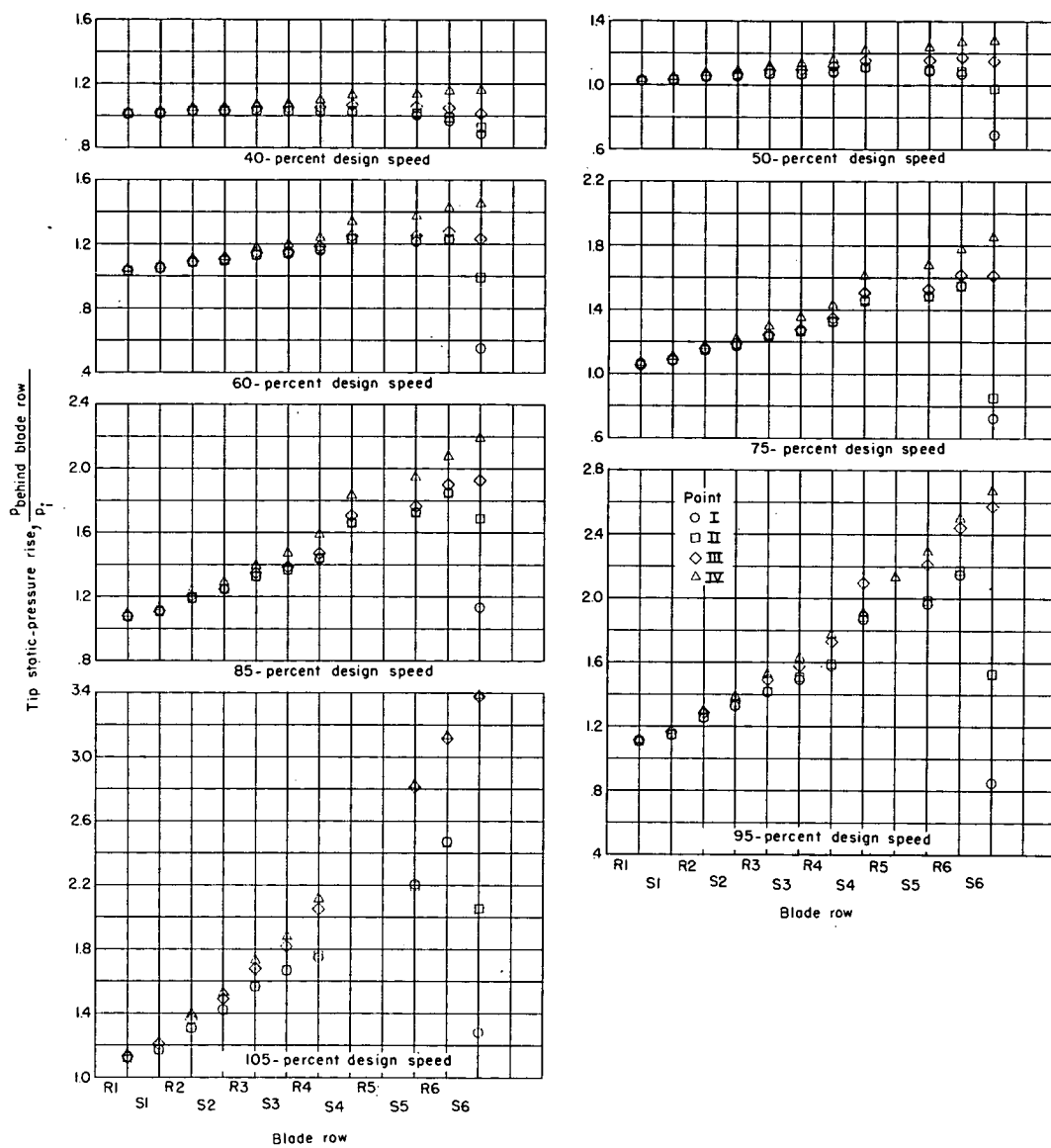
(b) Temperature efficiency (numerical average) as a function of percent design mass flow.

Figure 8.- Continued.



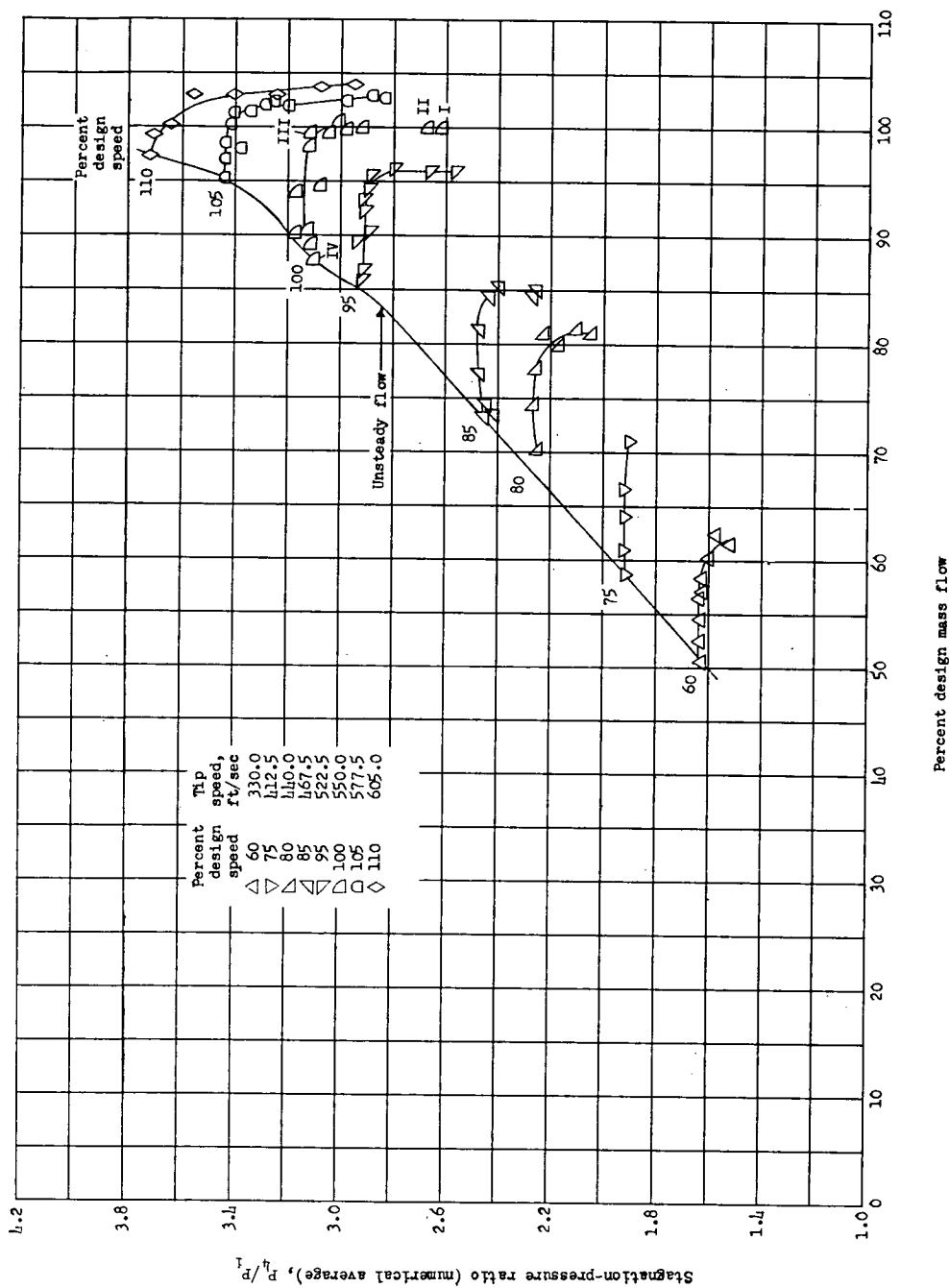
(c) Tip static-pressure rise as a function of blade row.

Figure 8.- Continued.



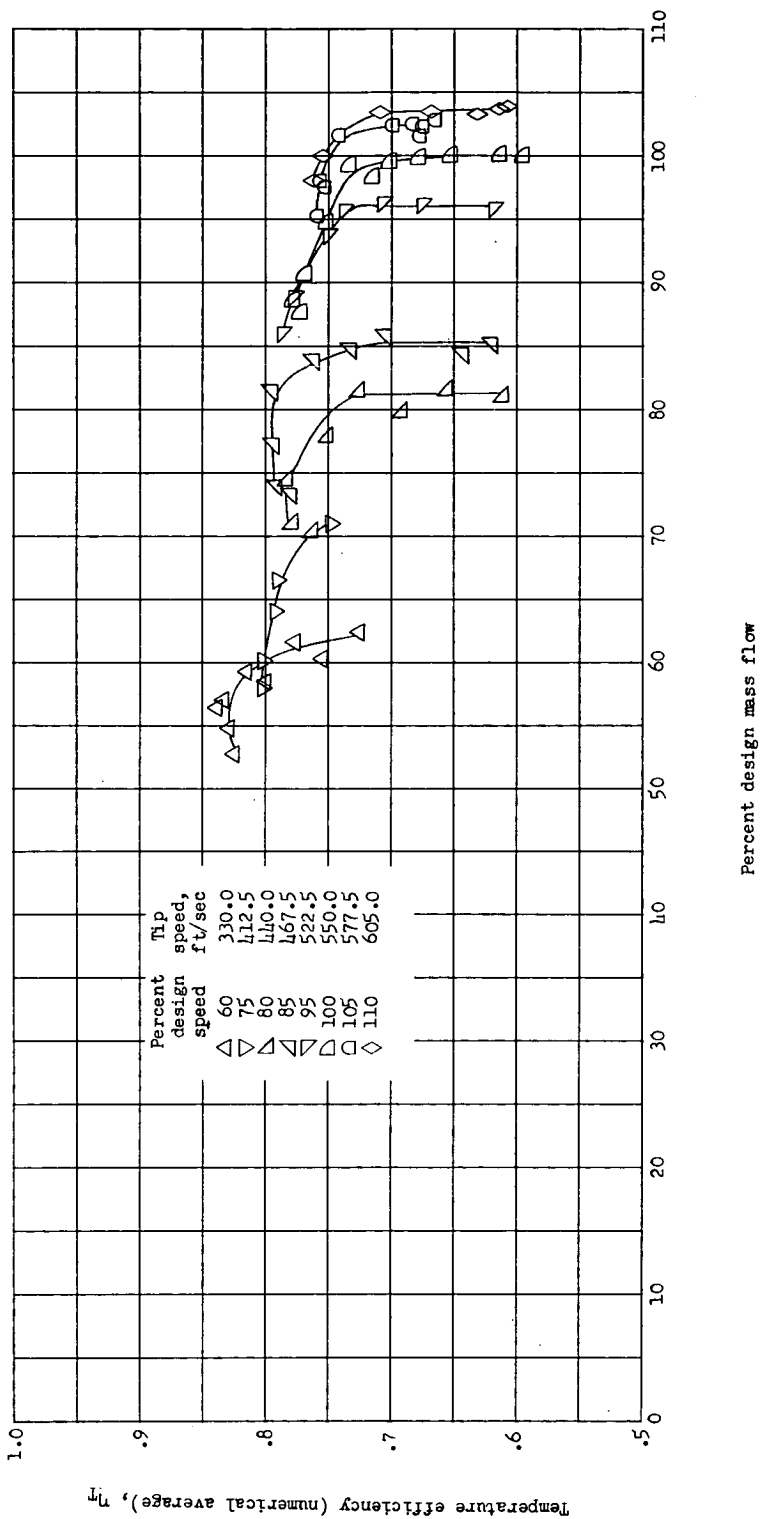
(c) Concluded.

Figure 8.- Concluded.



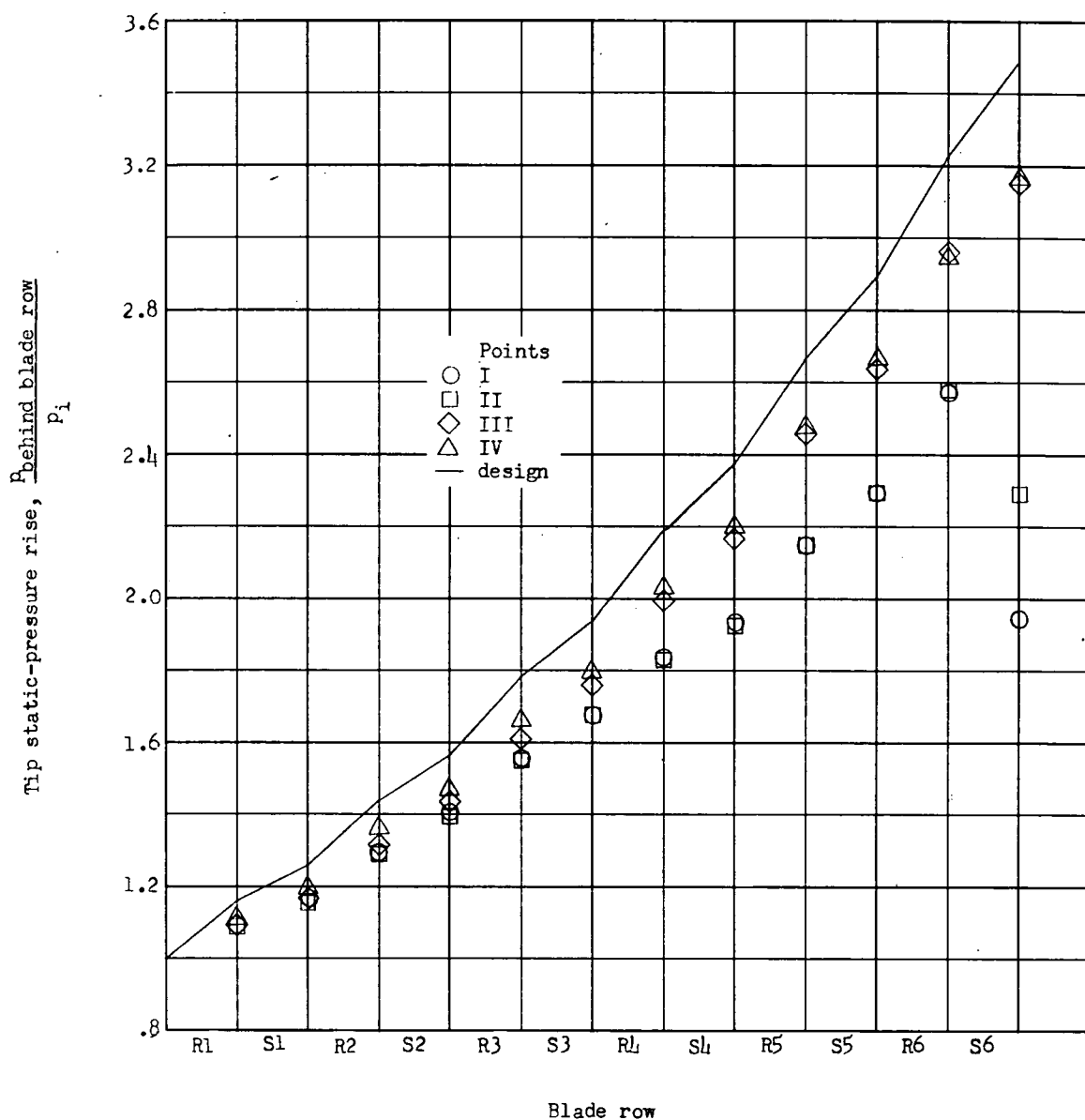
(a) Stagnation-pressure ratio (numerical average) as a function of percent design mass flow.

Figure 9.- Overall performance of a six-stage axial-flow compressor in air. Configuration B.



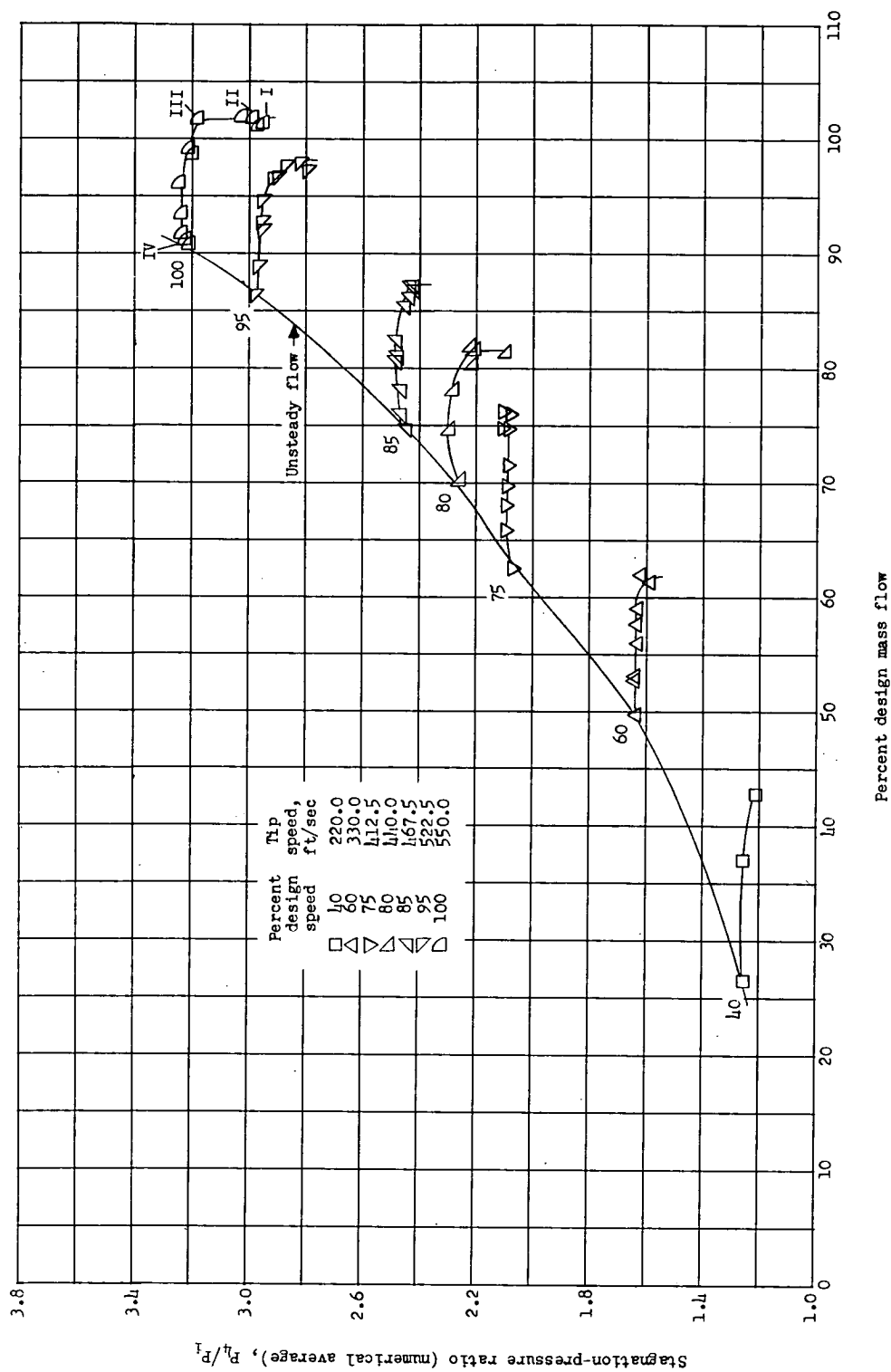
(b) Temperature efficiency (numerical average) as a function of percent design mass flow.

Figure 9.- Continued.



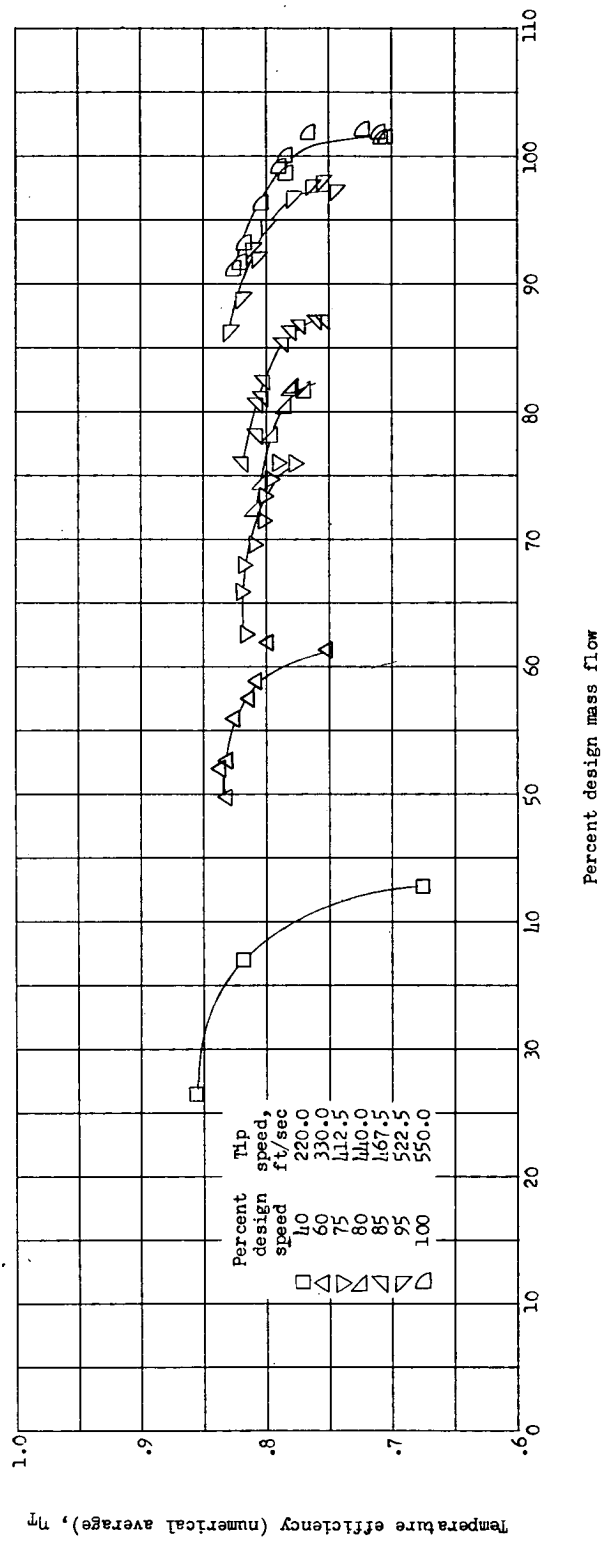
(c) Tip static-pressure rise as a function of blade row at 100 percent of design speed.

Figure 9.- Concluded.



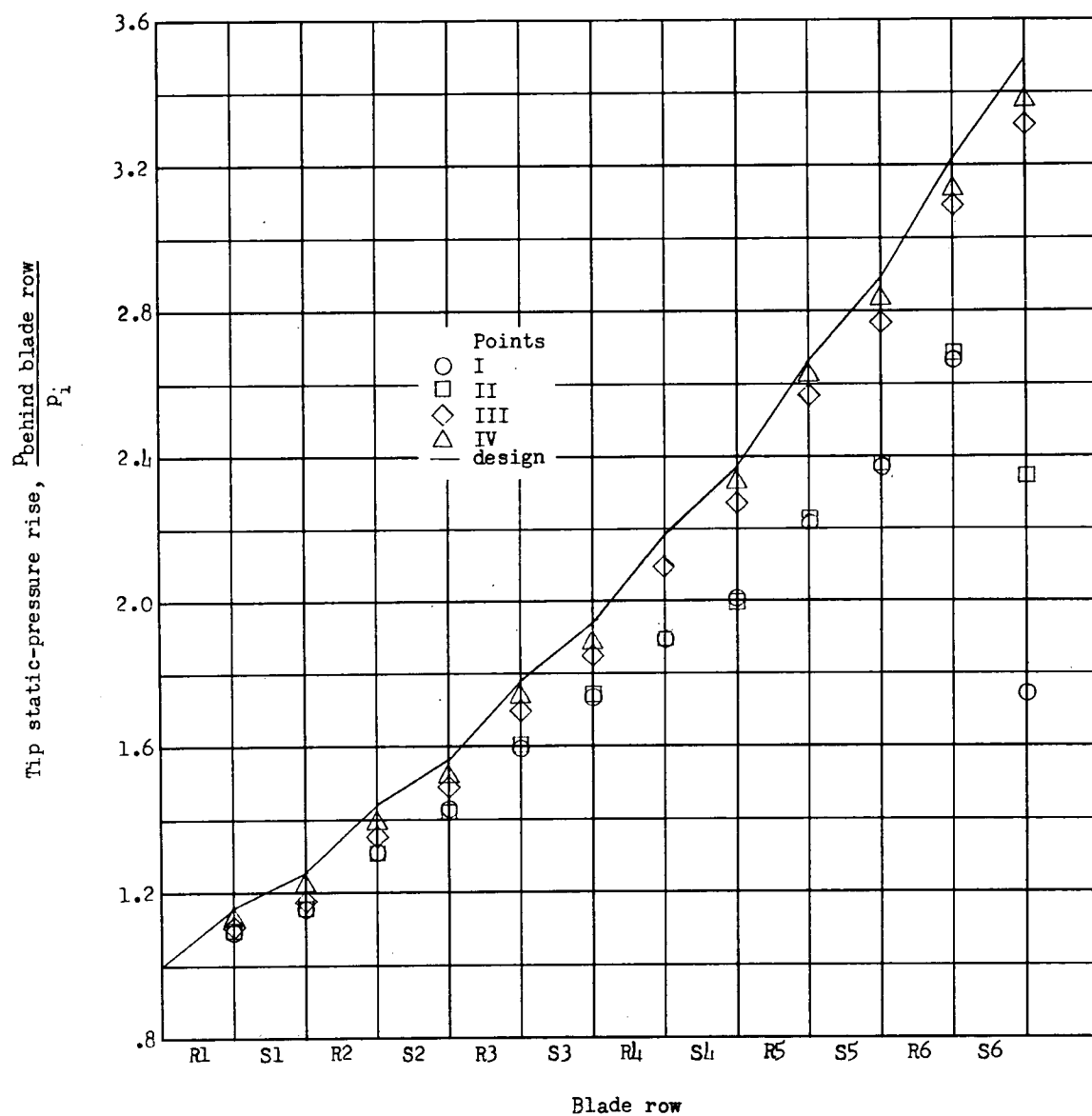
(a) Stagnation-pressure ratio (numerical average) as a function of percent design mass flow.

Figure 10.- Overall performance of a six-stage axial-flow compressor in air. Configuration C.



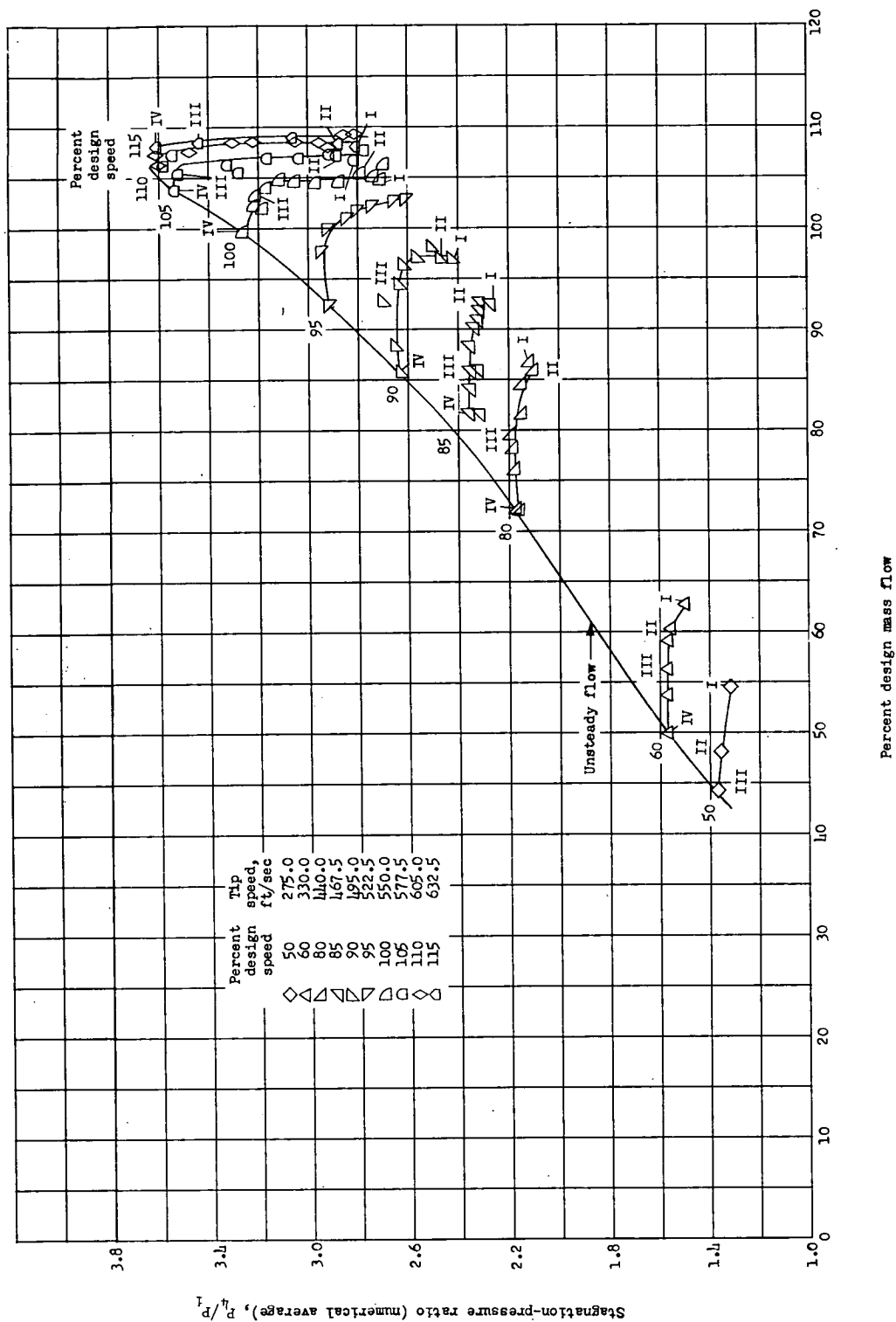
(b) Temperature efficiency (numerical average) as a function of percent design mass flow.

Figure 10.- Continued.



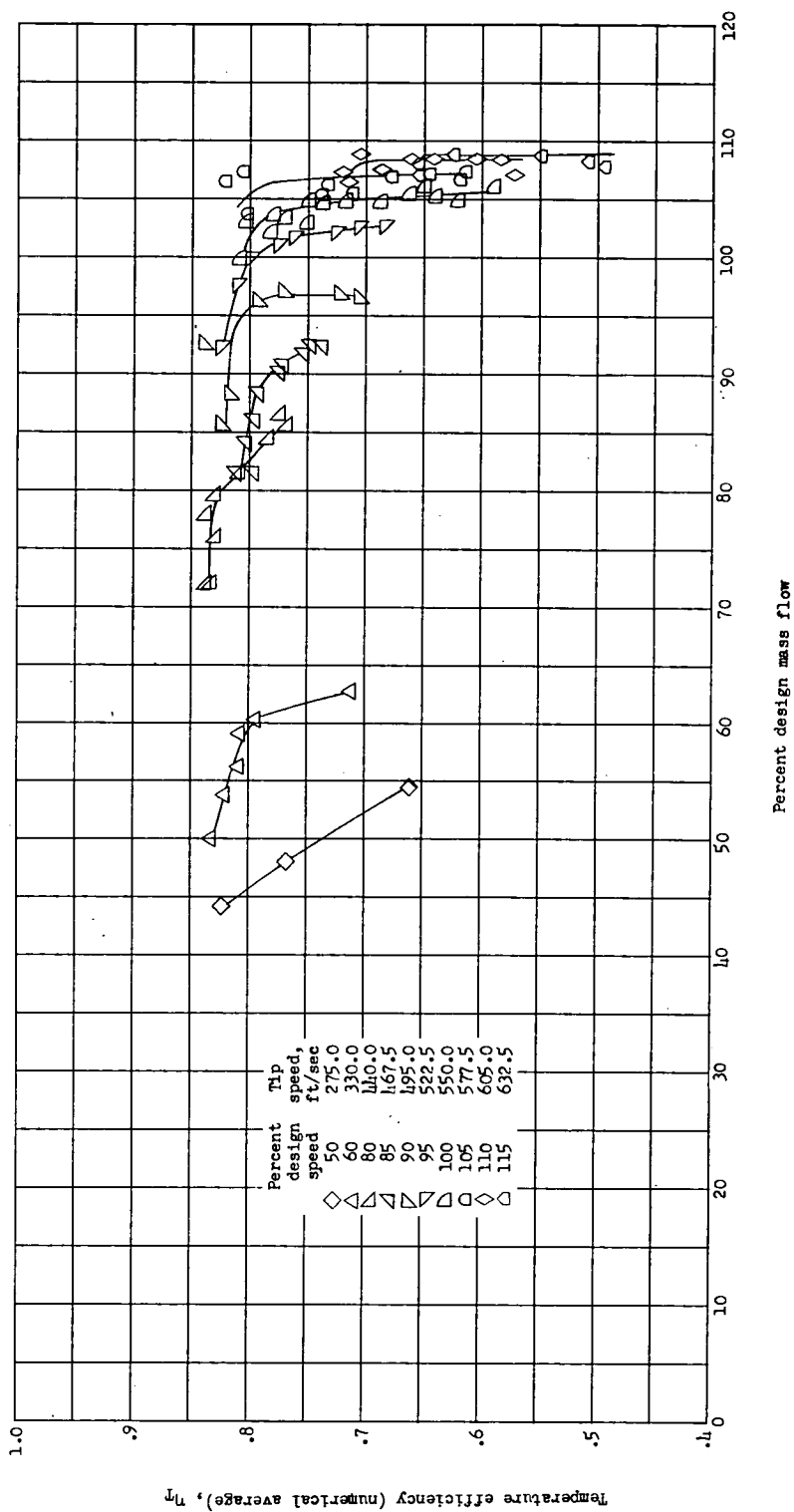
(c) Tip static-pressure rise as a function of blade row at 100 percent of design speed.

Figure 10.- Concluded.



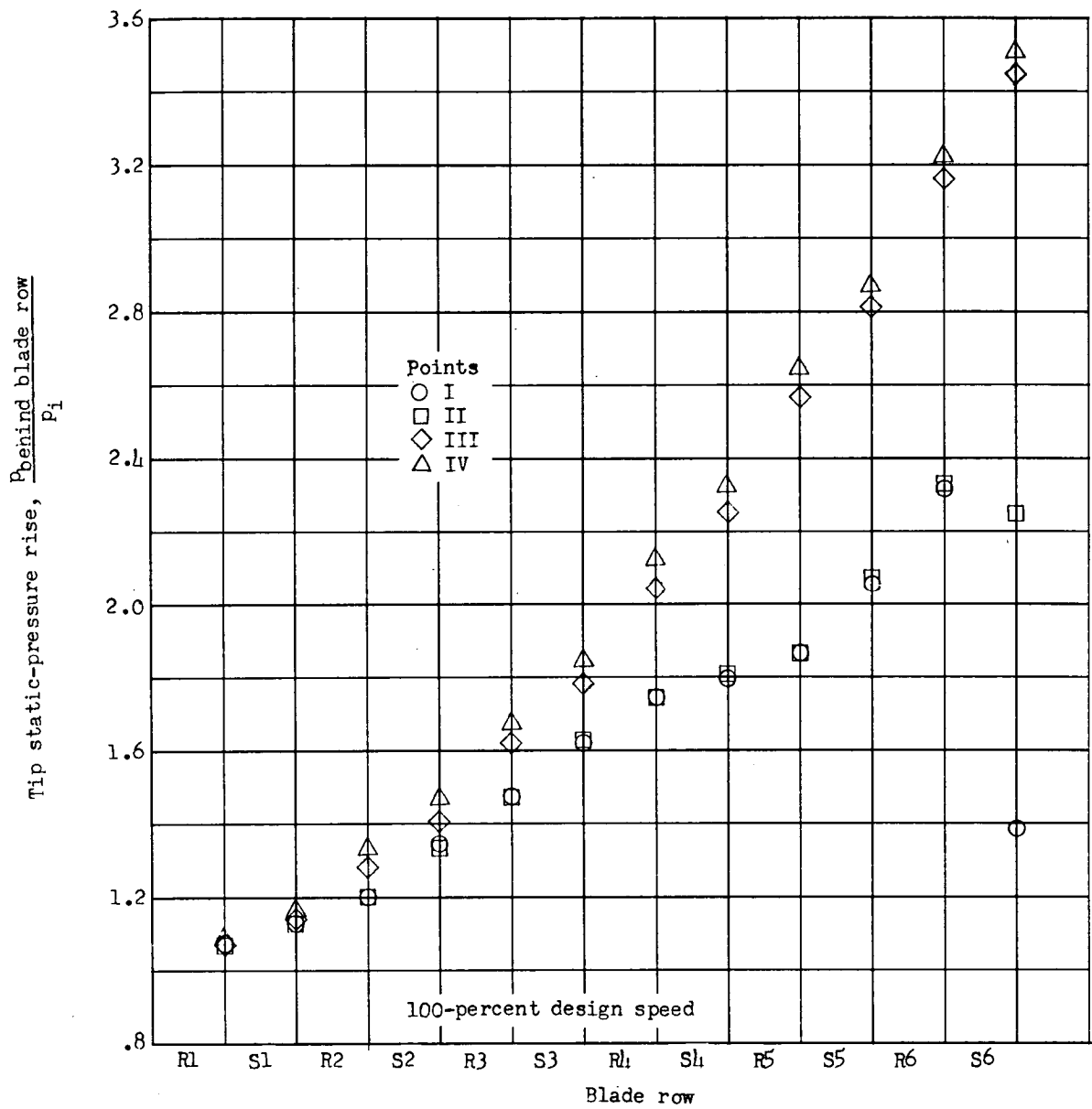
(a) Stagnation-pressure ratio (numerical average) as a function of percent design mass flow.

Figure 11.- Overall performance of a six-stage axial-flow compressor in Freon-12. Configuration C.



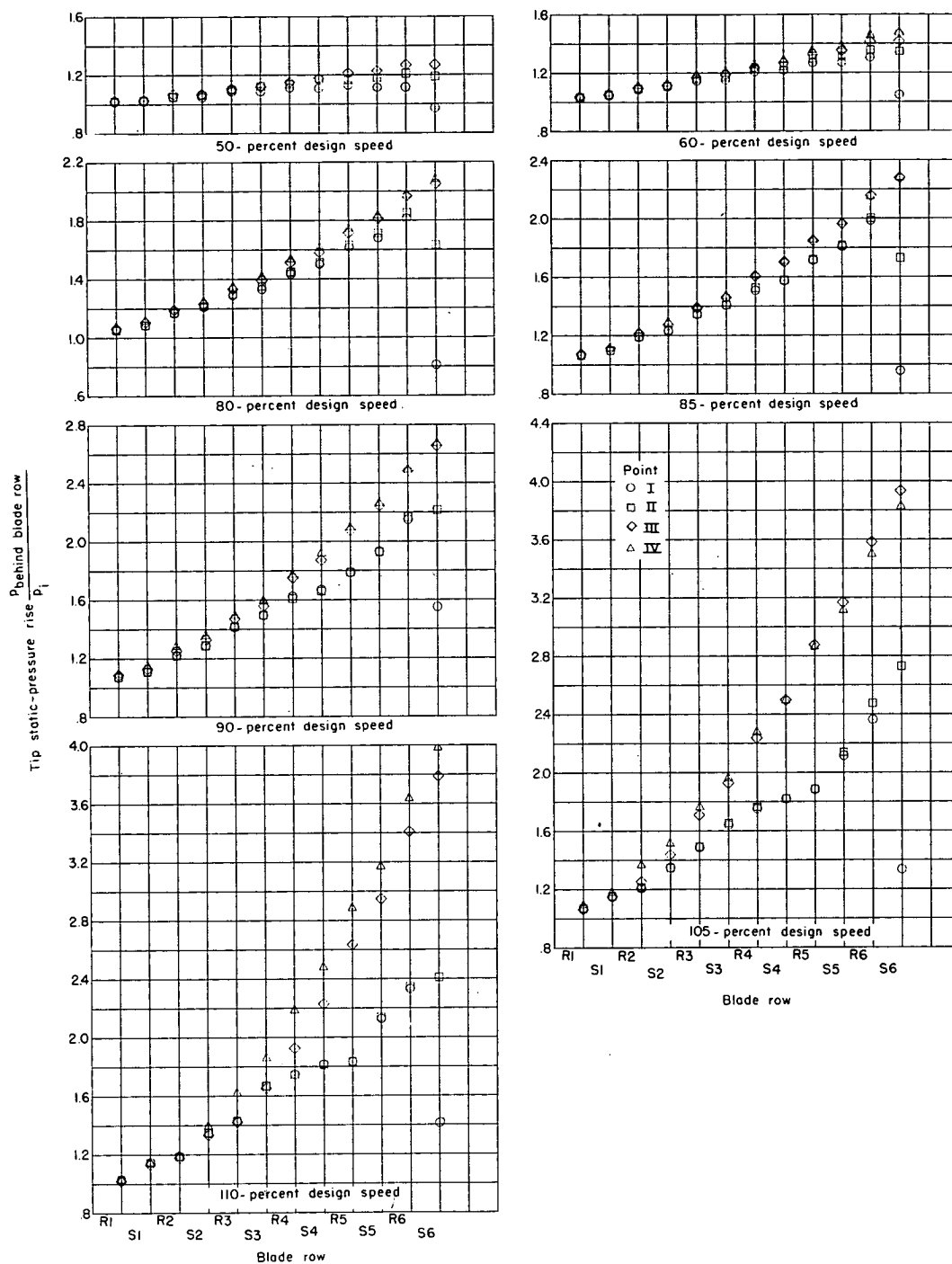
(b) Temperature efficiency (numerical average) as a function of percent design mass flow.

Figure 11.- Continued.



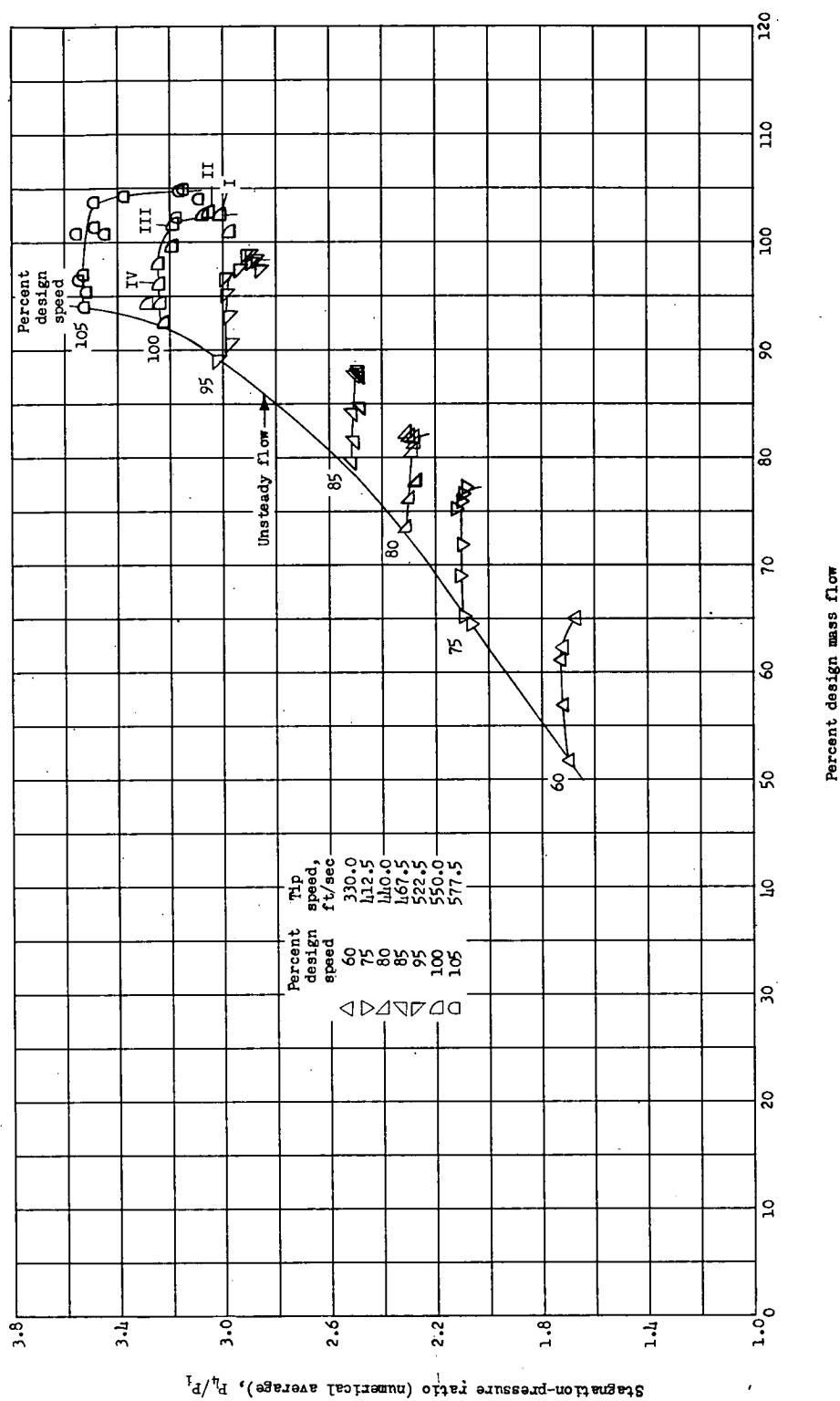
(c) Tip static-pressure rise as a function of blade row.

Figure 11.- Continued.



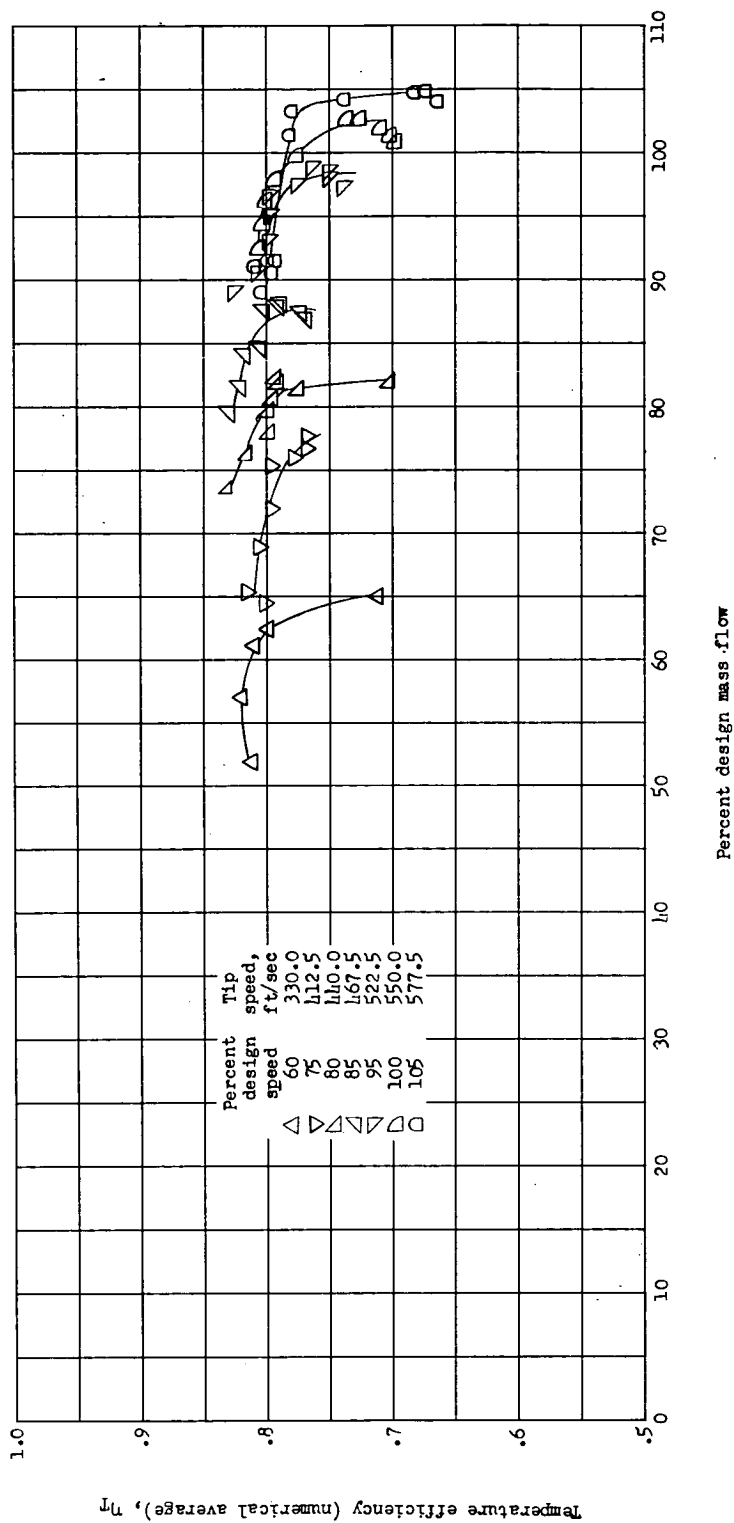
(c) Concluded.

Figure 11.- Concluded.



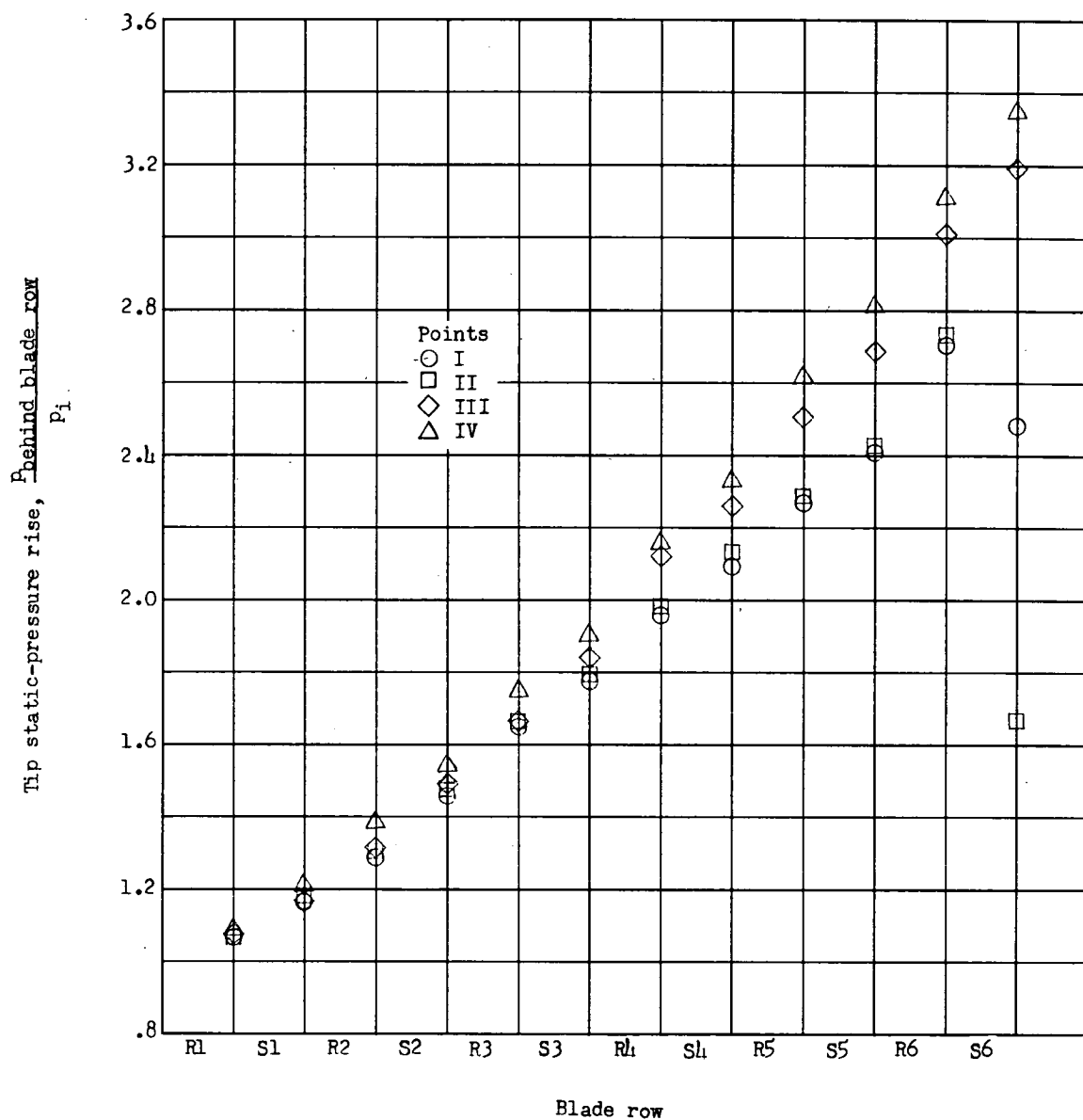
(a) Stagnation-pressure ratio (numerical average) as a function of percent design mass flow.

Figure 12.- Overall performance of a six-stage axial-flow compressor in air. Configuration D.



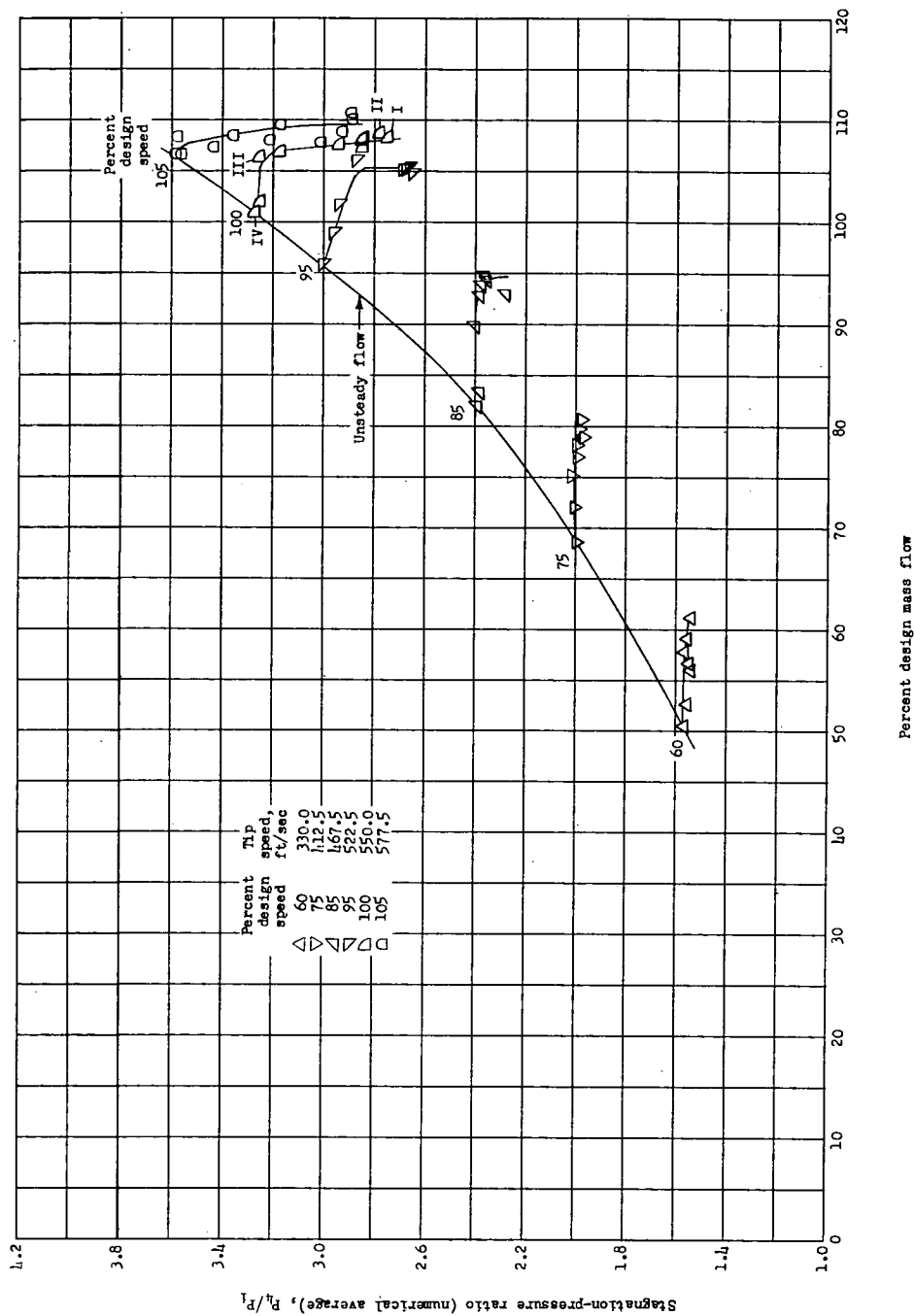
(b) Temperature efficiency (numerical average) as a function of percent design mass flow.

Figure 12.- Continued.



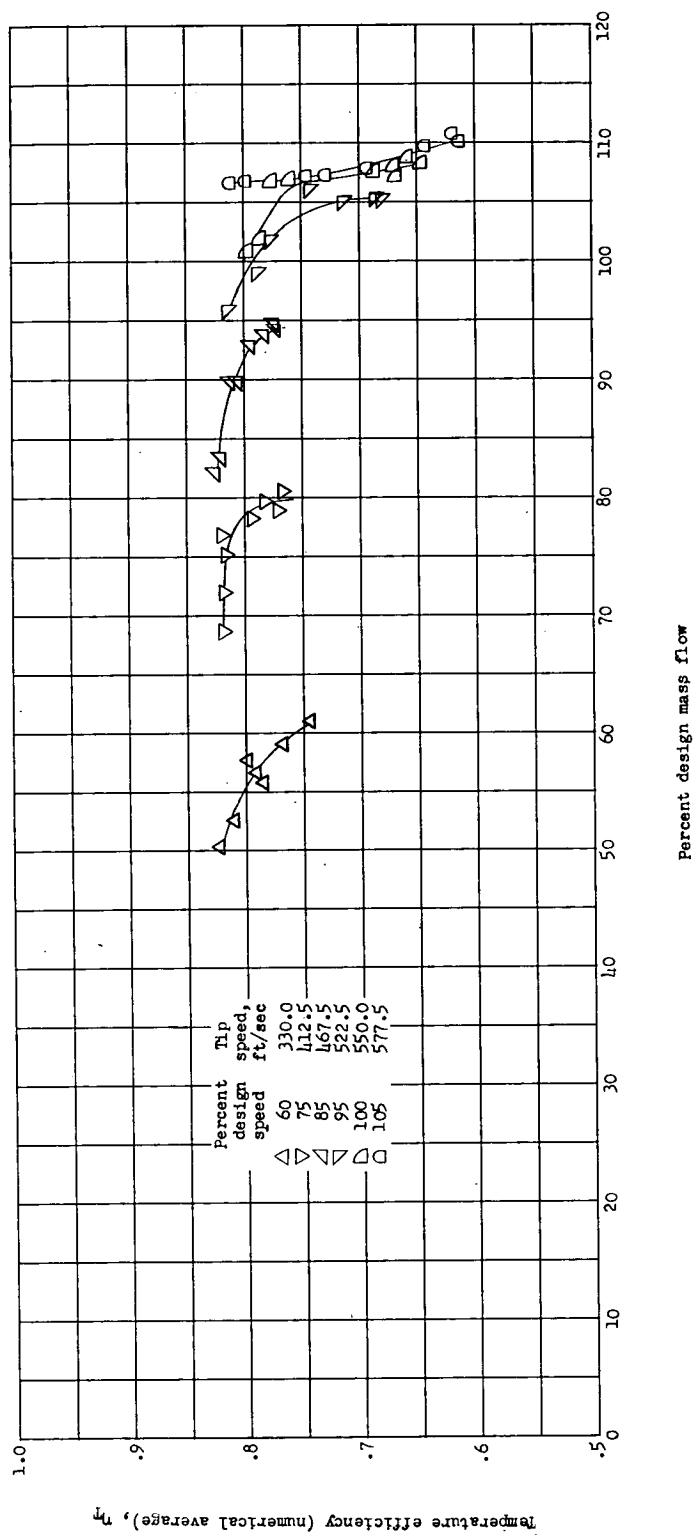
(c) Tip static-pressure rise as a function of blade row at 100 percent of design speed.

Figure 12.- Concluded.



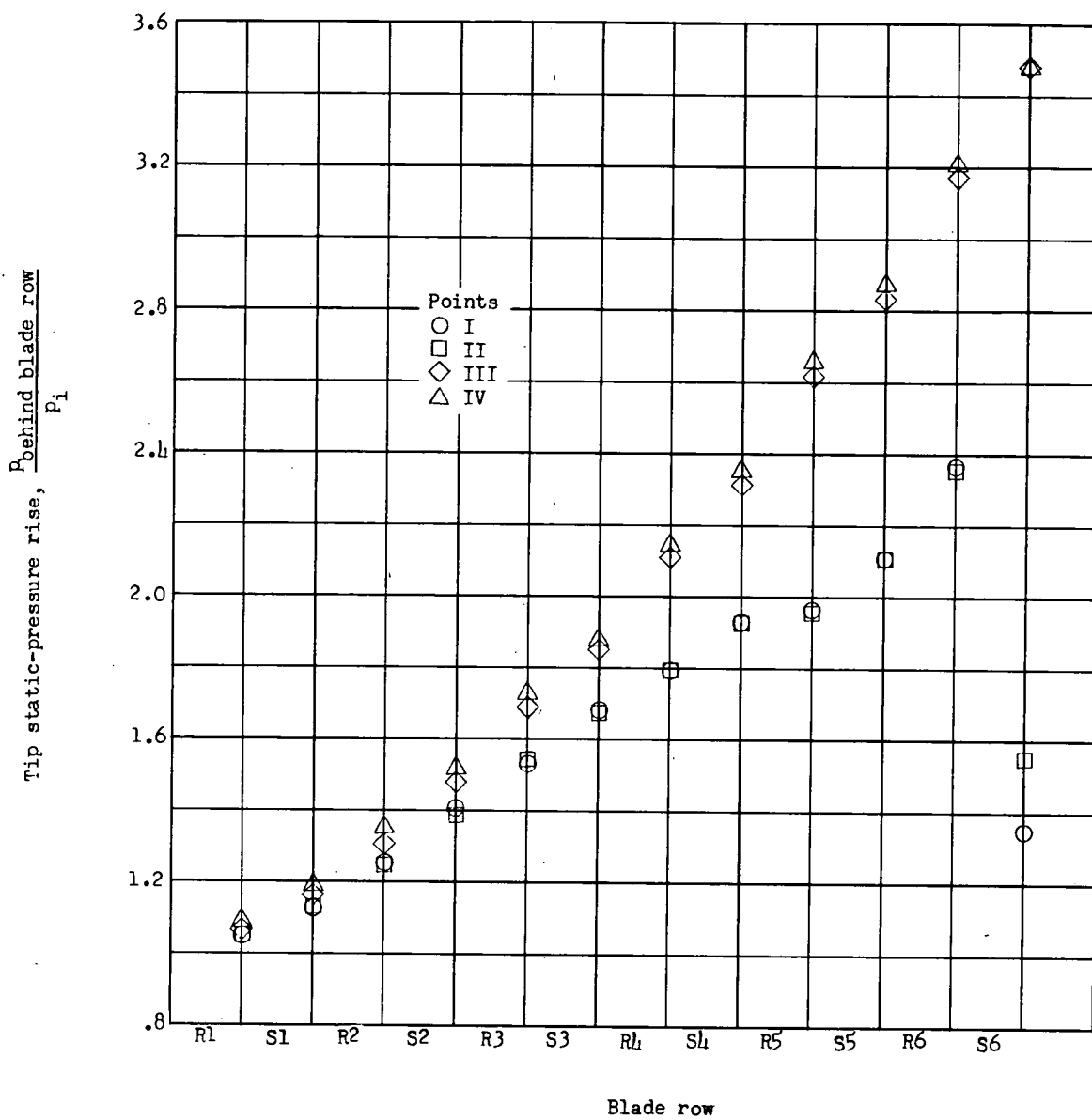
(a) Stagnation-pressure ratio (numerical average) as a function of percent design mass flow.

Figure 13.- Overall performance of a six-stage axial-flow compressor in Freon-12. Configuration D.



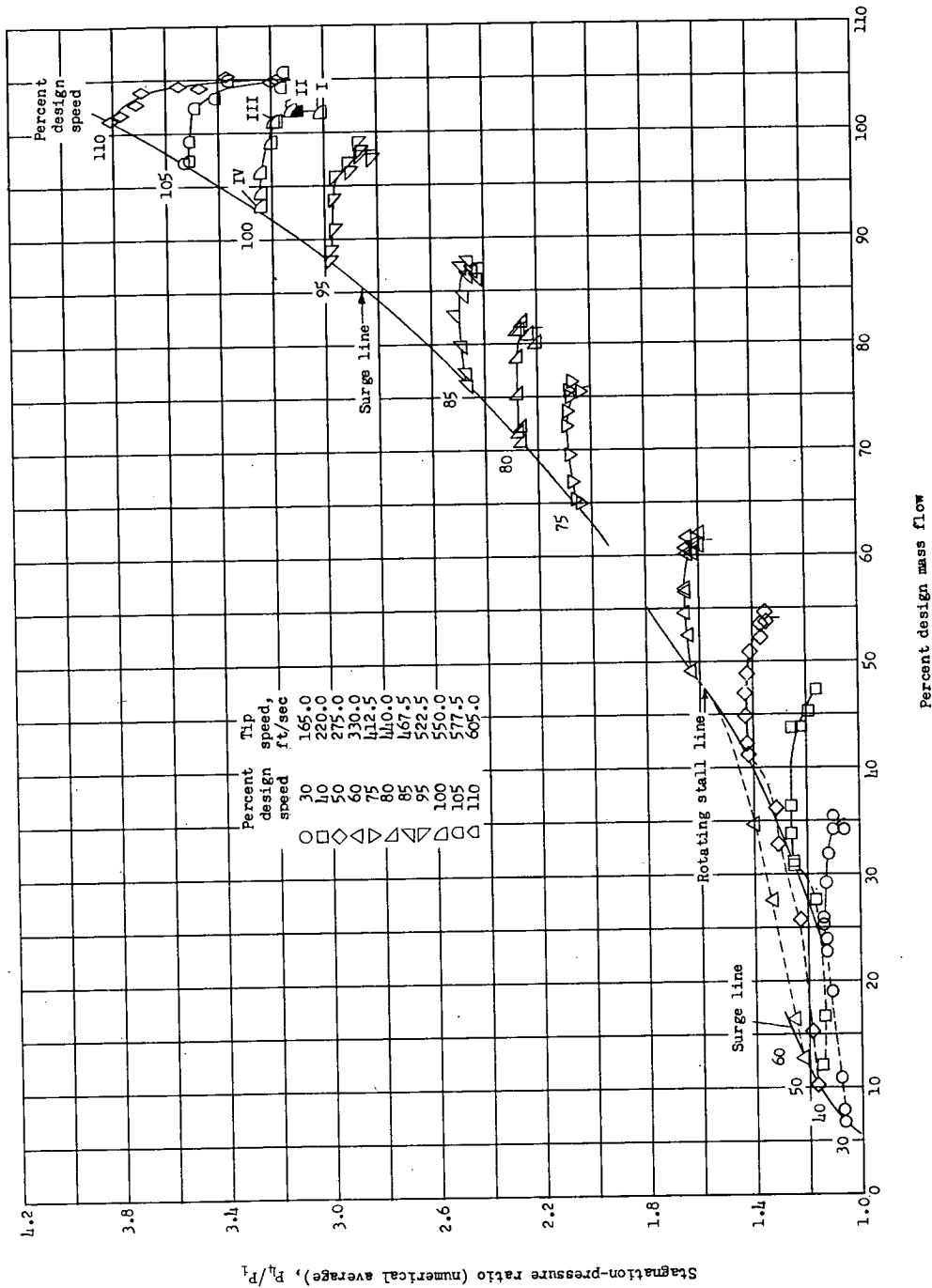
(b) Temperature efficiency (numerical average) as a function of percent design mass flow.

Figure 13.- Continued.



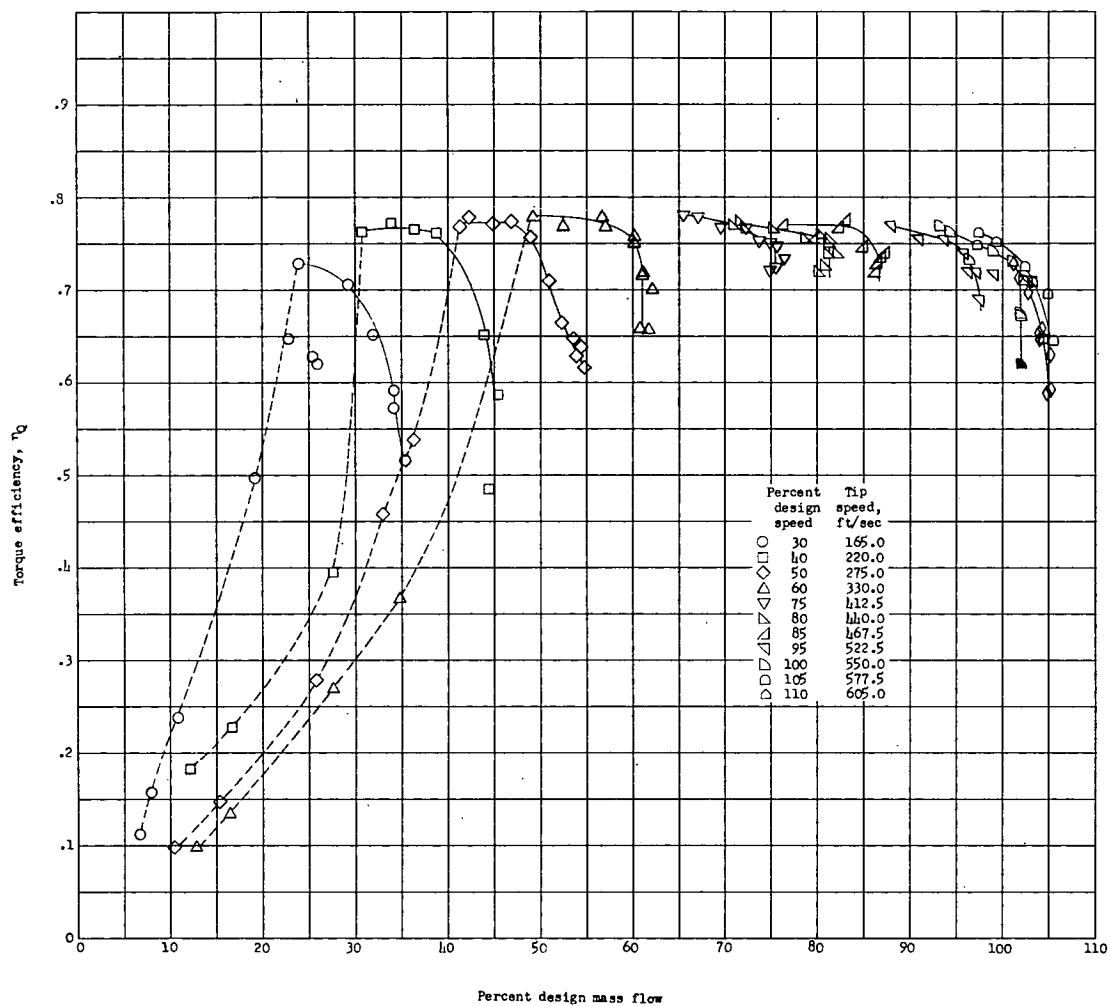
(c) Tip static-pressure rise as a function of blade row at 100 percent of design speed.

Figure 13.- Concluded.



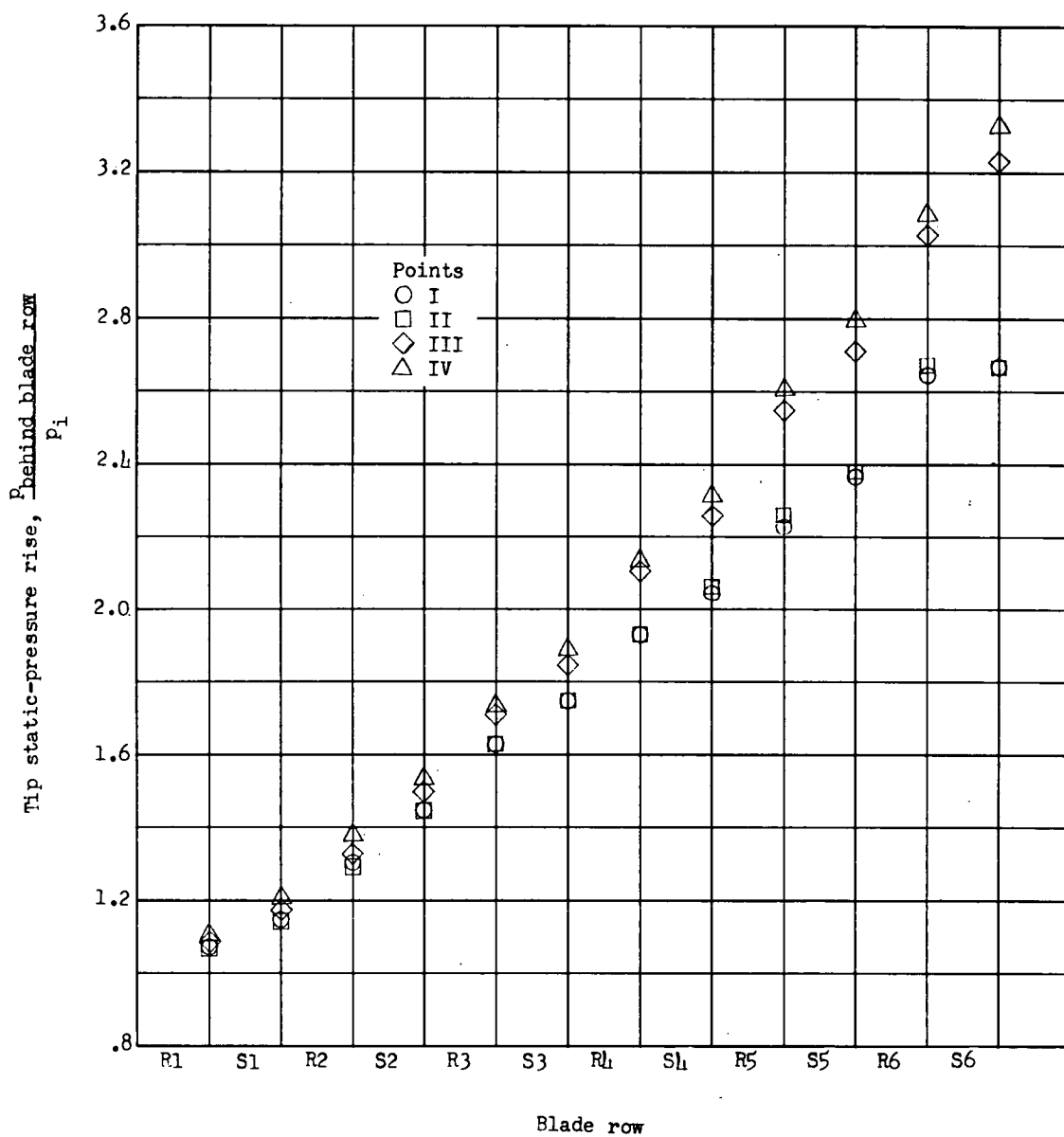
(a) Stagnation-pressure ratio (numerical average) as a function of percent design mass flow.

Figure 14.- Overall performance of a six-stage axial-flow compressor in air. Configuration E.



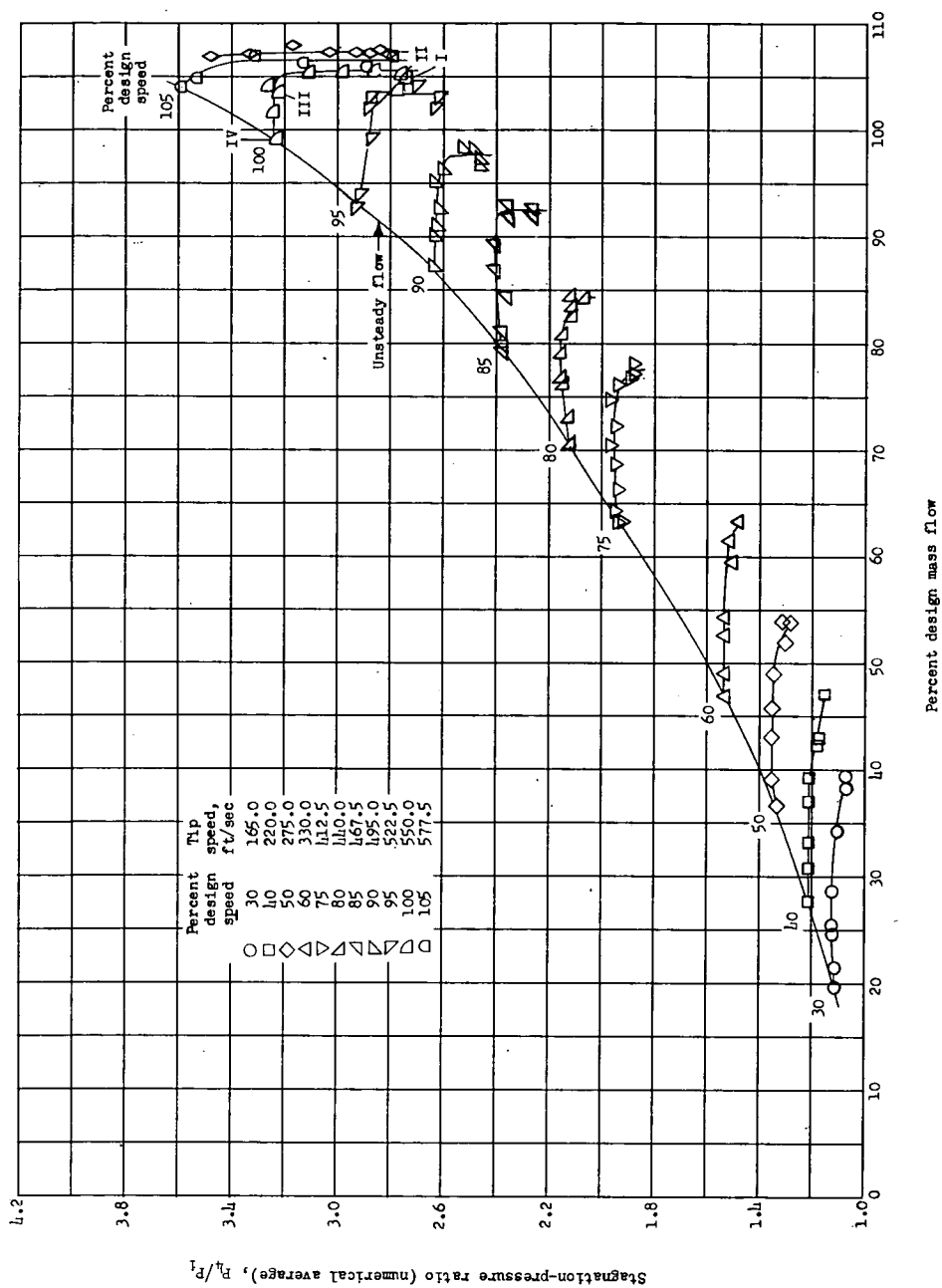
(b) Torque efficiency as a function of percent design mass flow.

Figure 14.- Continued.



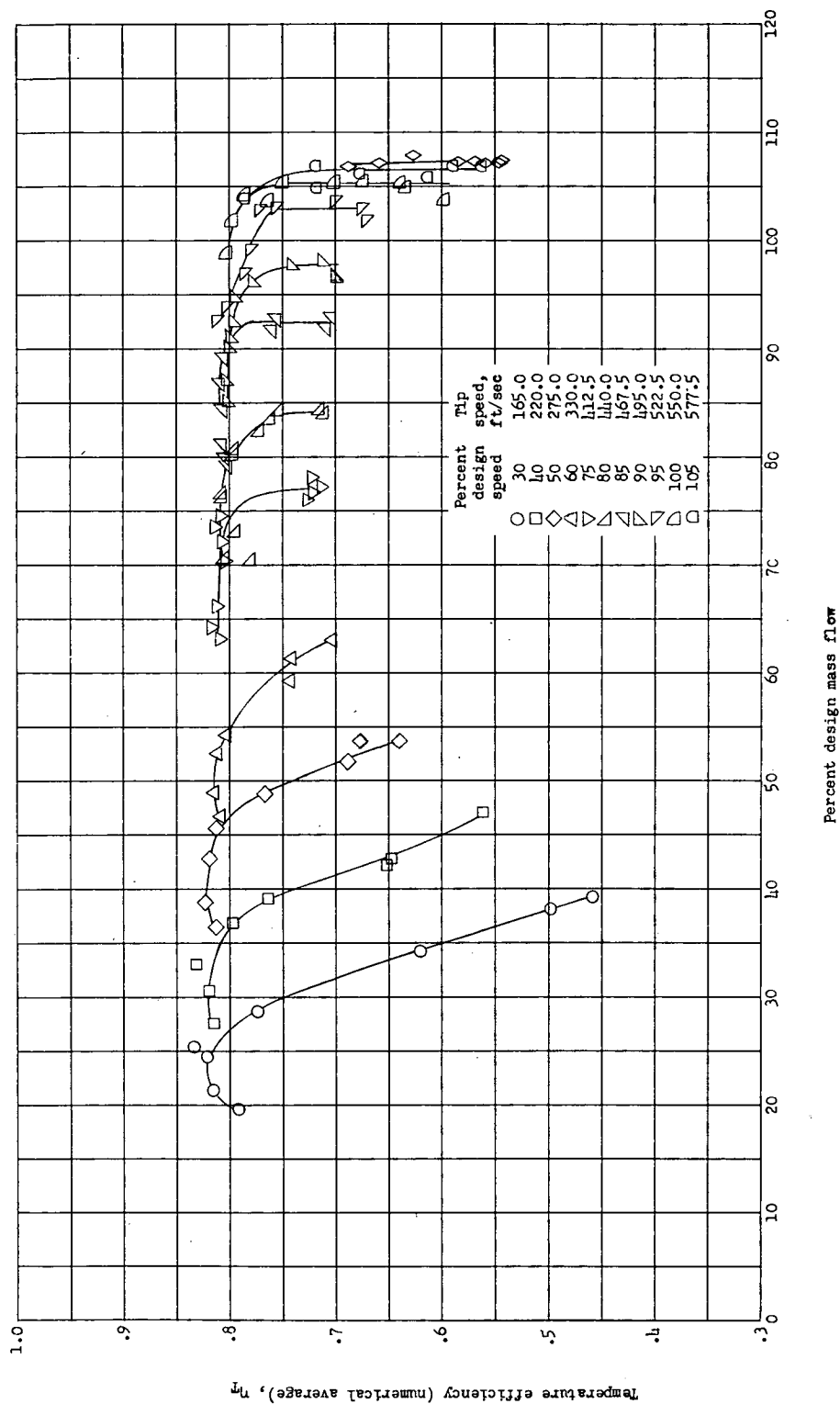
(c) Tip static-pressure rise as a function of blade row at 100 percent of design speed.

Figure 14.- Concluded.



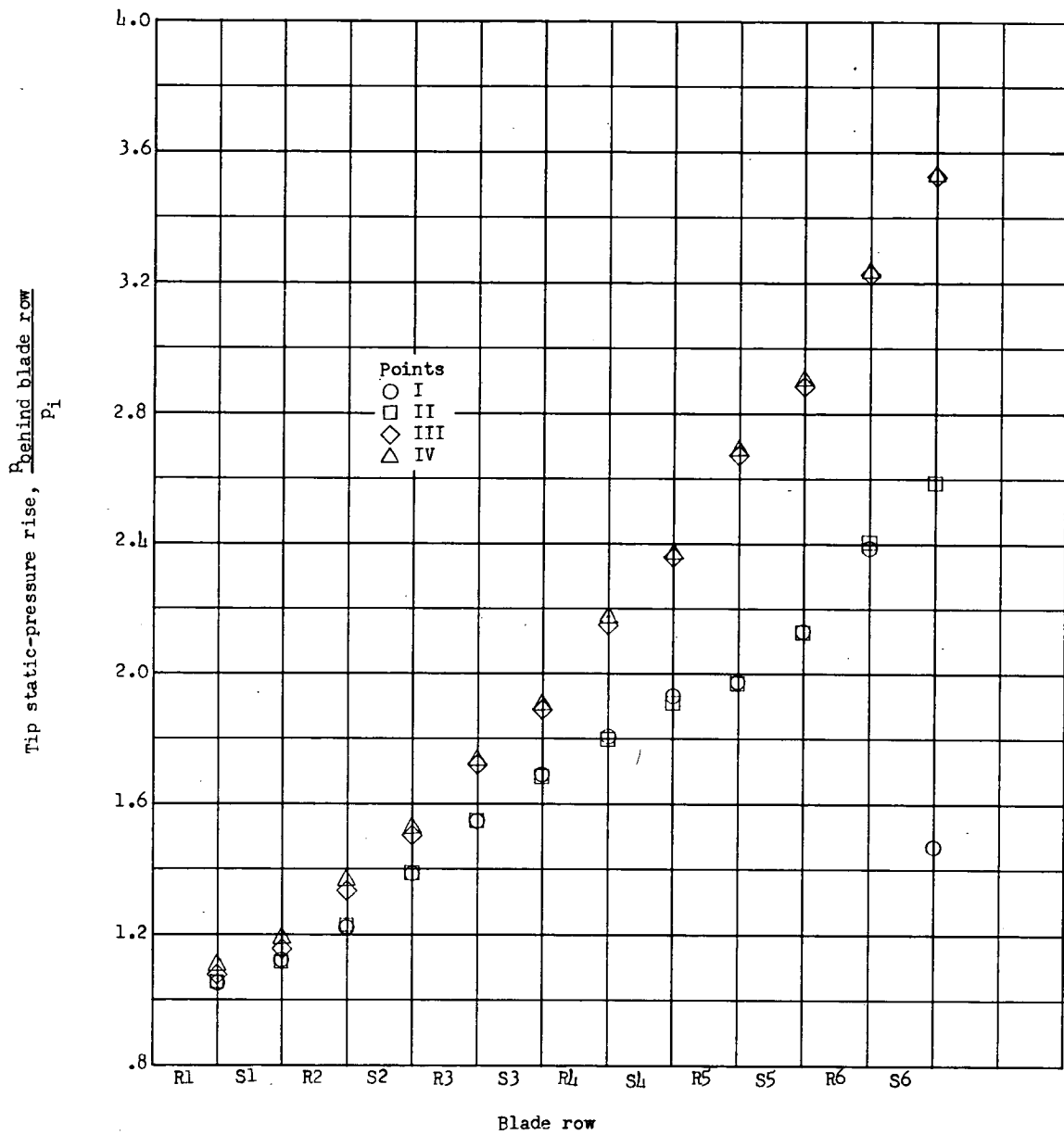
(a) Stagnation-pressure ratio (numerical average) as a function of percent design mass flow.

Figure 15.- Overall performance of a six-stage axial-flow compressor in Freon-12. Configuration E.



(b) Temperature efficiency (numerical average) as a function of percent design mass flow.

Figure 15.- Continued.



(c) Tip static-pressure rise as a function of blade row at 100 percent of design speed.

Figure 15.- Concluded.